Setup of Dry Cryostat for Measurements on Superconducting Microwave Resonators

by

Nicholas Aaron Cockton

A thesis
presented to the University of Waterloo
in fulfillment of the
thesis requirement for the degree of
Master of Science
in
Physics

Waterloo, Ontario, Canada, 2019

Author's Declaration

I hereby declare that I am the sole author of this thesis. This is a true copy of the thesis, including any required final revisions, as accepted by my examiners.

I understand that my thesis may be made electronically available to the public.

Abstract

A cryogen-free cryostat was set up in order to perform measurements at ultra low temperatures. The setup involved the removal of an adiabatic demagnetization refrigerator (ADR) and replacing it with a dilution refrigerator system. The modified cryostat is able to provide continuous cooling power, enabling greater flexibility over the ADR in the type of low temperature experiments that can be performed. Condensation stages, main flow impedance and radiation baffles were designed, constructed and installed into the cryostat. Several general cryostat design considerations are also discussed. Condensation of the incoming ^{3}He - ^{4}He mixture utilizes only the cooling power of the two-stage pulse tube refrigerator. For a circulation rate of 120 μmols/sec, the base temperature of the cryostat is 70 mK with a cooling power of 33 μW of heat at 100 mK.

With this cryostat, a measurement system is developed for studying superconducting microwave resonators. Residual losses in these devices continue to impede their performance in applications such as ultra sensitive detectors and quantum computing. A microwave circuit consisting of coaxial cables, attenuators and amplifiers was installed on the cryostat to measure losses in these devices. Data analysis and fitting procedures were written in Python programming language to extract key resonator properties. Characterizing and understanding loss mechanisms for these devices will lead to improved materials and fabrication methods. This will ultimately result in losses that approach the fundamental limit set by the Mattis-Bardeen theory.

Acknowledgements

I must thank my advisor, Jan Kycia. Your expertise and enthusiasm makes the lab both an interesting and exciting place to work. Under your guidance, I have come to appreciate the attention to detail and scrutiny needed to make scientifically sound measurements and conclusions. Working in your lab has been an excellent learning experience and I am truly grateful for the opportunity.

I would like to thank Jeffrey Mason for teaching me how to operate numerous pieces of equipment in the lab. I would also like to thank past and present members of the Kycia Low Temperature Group: Jeffrey Mason, David Pomaranski, Clifford Plesha, Tianze Zou, and Taylor Fraser for their help and making the lab a fun place to work. Hiruy Haile of the machine shop deserves recognition for teaching me how to machine a wealth of components for the fridge. I would like to thank the NRC group for generously providing a second dilution unit. I would like to thank Loren Swenson from *D-Wave Systems, Inc* for guidance on the resonator measurement.

Finally, I would like to thank my family. My parents, Lee and Cheryl, and brother, Ryan, have supported me throughout my entire university career. Most of all, I need to thank my girlfriend Gillian for putting up with me through this whole process.

Dedication

To Gillian and Lily ♡

Table of Contents

List of Figures

Abbreviations

ADR adiabatic demagnetization refrigerator 9

BPTR basic pulse tube refrigerator 5

CPW co-planar waveguide 59

DR dilution refrigerator 12

FAA Ferric Ammonium Alum 10

GGG Gadolinium Gallium Garnet 10

GHS gas handling system 34

KF Klein Flansche 23

LNA low noise amplifier 75

OD outer diameter 25

OPTR orifice pulse tube refrigerator 7

PCB printed circuit board 74

PTR pulse tube refrigerator 5

Chapter 1

Motivation and Summary

The liquefaction of helium in 1908 by Heike Kammerlingh Onnes forever changed the definition of low temperature physics. All current low temperature techniques that operate below 10 K rely on helium as the refrigerant due to its low boiling point and ideal gas properties. The price of helium in the last few decades has monotonically increased, making it impractical to continuously purchase in large quantities. The recent advances in closed-cycle, cryocooler designs, such as the pulse tube refrigerator (PTR), has allowed temperatures below the boiling point of helium (4.2 K) to be reached. This advancement has enabled low temperature techniques that required liquid helium to now operate in a "dry" configuration. The first part of this work details the setup of a dry cryostat. In Chapter 2, an overview of the principle behind a pulse tube refrigerator (PTR), an adiabatic demagnetization refrigerator (ADR) and the ^{3}He - ^{4}He dilution refrigerator (DR) are discussed. Chapter 3 presents the implementation, design considerations and troubleshooting involved in the setup of a dry style DR.

Using the cryostat described above, the second part of this thesis details the setup of a characterization measurement for superconducting microwave resonators. In contrast to resonators made with normal metals, which have a large dissipation from conduction losses, superconducting resonators operate at cryogenic temperatures and can achieve very high quality factors. The high quality factors make them attractive in applications such as coupling to superconducting qubits for quantum computing applications [8], quantum-

1

limited parametric amplifiers [9] and microwave kinetic inductance detectors (MKID) for radio-astronomy applications [10]. However, losses at low temperatures from two-level systems (TLSs) continue to impede the optimal performance in these devices. Chapter 4 of this work introduces superconducting resonators and a brief history of probing the loss mechanisms in these devices. Chapter 5 discusses the TLS model and its relationship to losses observed in superconducting resonators. Chapter 6 presents the experimental work and data analysis performed to extract the resonance parameters and the figure of merit for these devices, the zero temperature dielectric loss tangent δ^0_{TLS}.

Part I

Setup of Dry Cryostat

Chapter 2

Low Temperature Techniques

The investigation of materials and devices at ultra low temperatures near absolute zero provides a pathway to understanding the intrinsic properties of nature. Currently several methods exist to achieve such low temperatures, each with their own advantages and disadvantages. A relatively small amount of equipment and manpower is needed to reach temperatures of one Kelvin and above. However, it is usually desirable to achieve temperatures much lower in the millikelvin (mK) regime. To attain such low temperatures, one must use either an adiabatic demagnetization refrigerator, ^{3}He refrigerator or a ^{3}He - ^{4}He dilution refrigerator.

Historically these techniques required cryogenic liquids (nitrogen and helium) to enable cooling down from room temperature. Constantly replenishing these cryogenic liquids while cold can be time consuming and costly. Helium in particular is obtained almost exclusively from helium-rich natural-gas sources. This unsustainable practice makes helium a very precious non-renewable resource. In recent years, the price of helium has increased steadily, making it more economically difficult to repeatedly obtain in large quantities.

Recently, cryogen-free cryocoolers have been able to achieve temperature below the boiling point of liquid Helium (4.2 K). This has enabled these historically "wet" refrigeration techniques to now operate in a "dry" configuration. A small caveat of these cryocoolers is unavoidable vibrations at the experimental cold stage. However, for many experiments the

vibration levels are small enough to be ignored. Thus, implementation of these cryocoolers has ultimately reduced the cool-down effort and cost.

2.1 Pulse Tube Refrigerator

The pulse tube refrigerator (PTR) has become a low temperature physicist's most valuable piece of equipment. It is the modern-day standard for achieving temperatures in the few Kelvin regime without the use of liquid helium. It is a closed cycle system that is, in general, maintenance free, reliable and very simple to install and operate. Its main advantage over other cyrocooler designs, such as a Gifford-McMahon (GM) or Stirling type cooler, is the complete absence of moving parts in the cold area. This keeps vibration levels to a minimum. In a present-day low temperature cryostat, a PTR is typically used as the first stage of cooling, whereas in the past, liquid helium in a dewar was needed. The thermodynamics involved in the modern PTR are beyond the scope of this work. Thus, only a brief overview of the basic operation and components will be discussed. A more detailed overview can be found in the text of Ventura and Risegari [11].

The first PTR was introduced in 1963 by Gifford and Longsworth and is known as the basic pulse tube refrigerator (BPTR) [12]. Figure. 2.1 shows a schematic of a GM-style BPTR. All cryocoolers require a mechanism to supply a pressure oscillation to the system. This can either be from a high frequency piston (Stirling style) or a low frequency compressor with rotating valve distributor (GM style). For PTRs that operate in the few Kelvin regime, the GM style is necessary due to an increased diffusion depth of the working gas within the regenerator [11]. The working gas used is helium due to its ideal gas properties and low condensation temperature. The major components of the GM type BPTR include: a compressor, high pressure hoses, a rotary valve, regenerator and pulse tube. The compressor supplies high and low pressures to the rotary valve. High pressure hoses connect the compressor to the rotary valve, which is located near the cryostat but with flexible hoses to reduce vibrations. The rotary valve distributes the gas supply between the high and low side of the compressor at a frequency of 1-2 Hz. The regenerator is composed of a high heat capacity material, which is designed to retain a relatively high heat
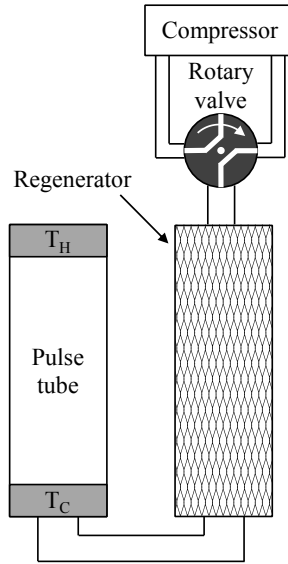
Figure 2.1: Schematic of GM style basic pulse tube refrigerator (BPTR).

capacity at low temperatures. Examples of regenerator materials used include phosphor bronze wire mesh, lead balls or rare earth magnetic materials [11]. The regenerator is responsible for storing heat absorbed from the gas before entering the pulse tube. The pulse tube is a hollow tube, allowing gas to be displaced from the cold end to the warm end.

The essence of the BPTR operation is simple: a compressor drives continuous oscillations of the pressure and displacement of the working gas inside the regenerator/pulse tube. It relies on the effect of surface heat pumping, where heat is exchanged between the working gas and the walls of the regenerator/pulse tube. Heat absorbed by the gas at the cold end of the pulse tube (T_C) is moved (pumped) to the hot end (T_H) where it is released. The simplified operation of the BPTR can be explained by considering the gas in the pulse tube during one complete cycle. During the compression cycle, extra gas flows in from the regenerator and acts like a piston to compress the gas initially in the pulse tube towards the hot end (T_H). The compression of the gas results in a higher pressure and temperature. The heat from compression is released into the heat exchanger and the resulting gas temperature drops. Before equilibrium can be established, the gas flow is

6

reversed, resulting in adiabatic expansion which further reduces the temperature of the gas. When the gas has expanded, it absorbs heat from the walls of the regenerator/pulse tube. This cycle is repeated with the temperature of the cold end of the pulse tube (T_C) dropping an incremental amount after each cycle. Eventually base temperature is reached when the amount of heat removed equals the amount of heat applied to the cold stage. Multiple PTRs can be arranged together to reduce the base temperature even further. The coldest temperatures achieved with the BPTR are 124 K for a single-stage and 79 K for a dual-stage [11].

In 1984, Mikulin *et al.* [13] introduced the modern, orifice pulse tube refrigerator (OPTR). The OPTR has the same components as the BPTR but with the addition of an orifice followed by a large reservoir (buffer volume) located at the warm end of the pulse tube. In contrast to a BPTR, surface heat pumping in an OPTR is actually a negative effect that is to be avoided. Instead, the principle of the orifice PTR relies on enthalpy transfer into the pulse tube from the regenerator and out through the orifice at the hot end of the pulse tube [14]. The combination of the orifice and the reservoir provide a phase shift between the gas flow and the pressure oscillation in the pulse tube and is crucial for the OPTR operation. Additional orifices were added by Zhu *et al.* in 1990 to increase efficiency and prevent losses at low temperatures [15]. These secondary orifices allow a small amount of gas to bypass the regenerator and enter the warm end of the pulse tube directly. It was found that only a fraction of the gas entering the regenerator contributes to cooling power. Thus, the secondary orifices reduce the heat load on the regenerator, resulting in a lower base temperature. Even though temperatures below the boiling point of ^{4}He are reached in modern OPTRs, no liquid-gas interface exists inside the system because the operating pressure (10-20 atm) is above the critical pressure of ^{4}He (2.25 atm) [2].

In this work, a Cryomech (model: PT410) PTR was used. The design and arrangement for this specific model appears to be a dual stage, parallel arrangement, double orifice, GM type PTR. Figure. 2.2 shows the schematic of the PT410. From the specification sheet, the nominal base temperature is 2.5 K (2nd stage) with a cooling power of 1.0 W at 4.2 K (2nd stage) and 40 W at 45 K (1st stage).
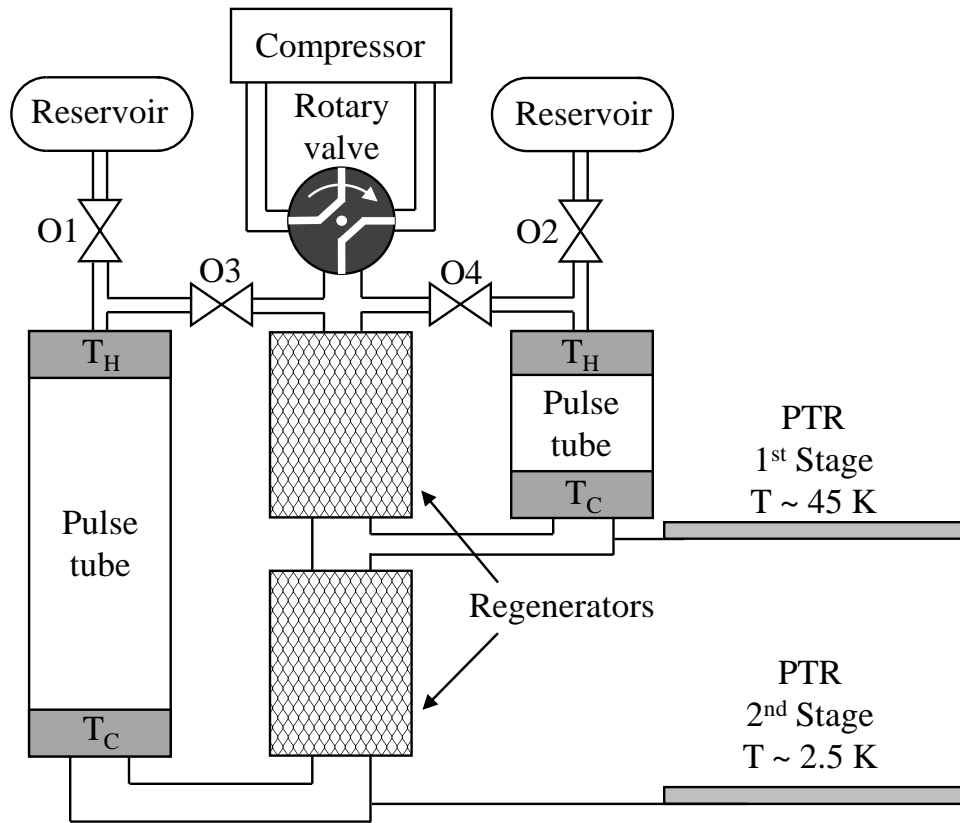
Figure 2.2: Schematic of the Cryomech PT410 dual stage, parallel arrangement, double orifice, GM style PTR used in this work. Orifices O1 and O2 and the two reservoirs provide a phase shift between the gas flow and the pressure oscillation in the pulse tube. Orifices O3 and O4 allow gas to bypass the regenerator and enter the warm end of the pulse tube directly.

2.2   Magnetic Refrigeration

To motivate the work presented in the next chapter, it is useful for the reader to have a basis of the principle behind magnetic refrigeration. Cooling by magnetic refrigeration, proposed and harnessed in the 1920s/1930s, was the first low temperature technique capable of reaching temperatures much less than one Kelvin. The modified cryostat described in chapter 3 was originally configured as an adiabatic demagnetization refrigerator (ADR), which relies on the magnetic refrigeration principle. An ADR is capable of reaching temperatures less than 100 mK, requiring very few pieces of equipment in comparison to a ^{3}He refrigerator or a ^{3}He - ^{4}He dilution refrigerator. In addtion, the cost of an ADR system is significantly less due the absence of ^{3}He from its operation. However, the ADR has one very significant limitation: finite cooling power over a short period of time (one-shot technique). This prohibits its use for experiments requiring long thermal time constants and/or long integration times. A very brief description of the ADR and its operation will be discussed. Further details can be found in the text of Pobell [2].

An ADR relies on the thermodynamic relationship between temperature and entropy. First, consider a paramagnetic material in the presence of an external magnetic field. A paramagnetic material has unpaired electrons. The magnetic moments of these unpaired electrons will align along the direction of the applied field but not retain any net polarization when the external field is removed. Assuming the thermal energy $k_B T$ is much larger than the interaction energy of the moments themselves, the moments can be considered to behave freely. The total entropy contribution of these free magnetic moments μ with total angular momentum J is given by

$$S = N k_B \ln(2J + 1) \tag{2.1}$$

where N is the number of molecules in the material. This magnetic entropy disorder is harnessed in an ADR system. The magnetic entropy within the material is reduced upon application of an external magnetic field. Entropy from other sources such as phonons or conduction electrons are relatively weak in comparison and can be neglected in this model.

To practically utilize this effect in an ADR system, a paramagnetic salt is first cooled

to a few Kelvin by a first stage, independent cooling mechanism. This mechanism can either be an isolated liquid helium bath, pumped ^{4}He reservoir or a PTR. As illustrated in Fig. 2.3, an external magnetic field is applied which polarizes the electronic magnetic moments in the salt. During this step, the salt undergoes isothermal magnetization, where heat is released into the first stage cooling mechanism. Once a set maximum magnetic field is reached, the total entropy of the salt is at a minimum value. By thermally decoupling the salt from the first stage cooling mechanism and reducing the external magnetic field, the salt undergoes adiabatic demagnetization. This in turn causes the temperature of the salt to decrease, which is connected to the experimental stage.

For the Shasta model 106 cryostat used in this work, the ADR component utilized a PTR to pre-cool the two paramagnetic salts, Ferric Ammonium Alum (FAA) and Gadolinium Gallium Garnet (GGG). To supply high magnetic field to the salts, a superconducting 4 Tesla magnet is employed. The salts are suspended inside the bore of the magnet by thermally isolating Kevlar supports. A mechanical switch is used to decouple the salts from the 2nd stage PTR during adiabatic demagnetization. The cooling capacity of each of these salts per demagnetization cycle is $\sim$ 100 mJ at 100 mK (FAA) and $\sim$ 1 J at 1 K (GGG) [1]. The finite cooling capacity of the salts makes the ADR an undesirable refrigeration method. It is for this reason that the cryostat was modified by removing the ADR component and replacing it with a ^{3}He -^{4}He dilution refrigerator.
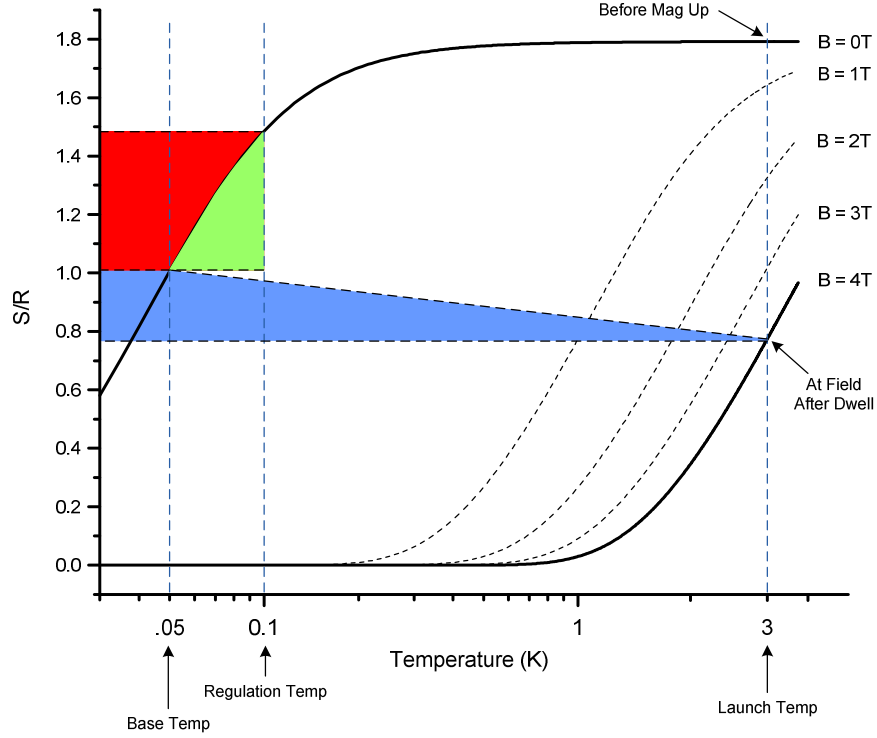
Figure 2.3: Entropy over R (Nk_B) as a function of temperature and time for the FAA paramagnetic salt used in the ADR. [1]. The salt begins at zero field and thermally connected to the PTR 2nd stage at the the point labelled "Before Mag Up". Application of an external field results in ordering of the magnetic moments in the salt (entropy is reduced), which releases heat into the PTR 2nd stage ("At Field After Dwell"). Thermally decoupling the salt from the PTR 2nd stage and reducing the field results in a reduction in temperature (horizontal dashed lines). The shaded blue area represents the energy absorbed from the mass connected to the FAA salt during demagnetization. For a complete demagnetization to zero field, the red shaded area represents the energy available by the salt. The demagnetization ramp can be stopped to regulate at a specific temperature (above base temperature). For a regulated warm up, the shaded green and red area represents the energy available by the salt.

11

2.3 The Dilution Refrigerator

The ^{3}He - ^{4}He dilution refrigerator (DR) is a marvel of physics and engineering. Initially proposed and realized in the 1950s/1960s, DRs are still the only way to achieve continuous cooling power below 0.3 K. This is highly desirable as it eliminates the measurement time and heat load constraint found in ADR refrigeration systems. Over the years, the design of the DR has changed very little. The most significant change is the complete elimination of consumed cryogenic liquids (nitrogen and helium) from its operation. This is done by utilizing a PTR as the first stage of cooling. This has reduced the operational cost while also creating a self-sufficient system. In this work, a dry DR setup was built, the details of which will be described in Chapter 3. First, a brief theoretical overview of the operational principle behind the DR will be discussed. Further details not disussed here can be found in the text of Pobell [2].

2.3.1 Refrigeration Mechanism

The cooling mechanism behind a DR is a result of mixing the two stable isotopes of helium, ^{3}He and ^{4}He, at low temperatures. As mentioned previously, ^{4}He is the most common helium isotope and is captured from helium-rich natural gas sources. ^{3}He, with one less neutron in its nucleus, is the only other stable helium isotope. While ^{3}He does exist in extremely limited concentrations in nature, for practical purposes it is instead produced in the decay (byproduct) of of tritium (^{3}H) manufacturing in a nuclear reactor. As a result, ^{3}He is extremely rare and precious. When ^{3}He is used in cryogenic refrigeration techniques, it is always used in a closed cycle system.

Before discussing the cooling mechanism, it is useful to outline the quantum properties that these two helium isotopes exhibit. At low temperatures and in the liquid state, quantum effects govern their behaviour such that they are referred to as quantum liquids. The quantum statistics they follow depend on the internal composition of their nuclei. The nucleus of ^{4}He has an even number of Fermions, containing two protons and two neutrons, resulting in a nuclear spin of zero. As a consequence, ^{4}He is a Boson and follows Bose-Einstein statistics. At saturated vapour pressure and below 2.177 K, a fraction of

^{4}He atoms undergoes Bose condensation to a superfluid state – a distinct phase of matter where a fluid flows with zero viscosity and thus flows without the loss of kinetic energy. On the contrary, the nucleus of ^{3}He has an odd number of Fermions, containing two protons and only one neutron. The absence of this neutron gives a nuclear spin of $1/2$, making ^{3}He a Fermion and instead following Fermi-Dirac statistics. Similarly, ^{3}He atoms can group into pairs, analogously to electron pairing in a superconductor. These ^{3}He atom pairs, which have a net integer spin, can then also Bose condense form a superfluid state for temperatures below 2.491 mK, at saturated vapour pressure.

The electronic structure of both isotopes is the same and consists of a closed s-shell. This results in extremely weak van der Waals forces between atoms. In addition, the zero-point energy is relatively large due to the small atomic masses of the two isotopes. The zero-point energy is given by

$$E_0 = \frac{h^2}{8ma^2} \tag{2.2}$$

where a describes the relative size of the sphere occupied by the atoms. For ^{3}He, with an even smaller mass than ^{4}He, this effect is even more pronounced. Some obvious consequences as a result of these properties are: low boiling points at saturated vapour pressure (4.23 K for ^{4}He, 3.19 K for ^{3}He), low critical temperatures, low densities, low latent heats of evaporation and large vapour pressures.

Mixing these quantum liquids at low temperatures results in interesting behaviour. Fig. 2.4 shows the phase diagram of liquid ^{3}He -^{4}He below 2 K. ^{3}He - ^{4}He mixtures with a ^{3}He concentration of 6.6% or more will eventually phase separate into a ^{3}He rich phase and a ^{3}He dilute (^{4}He rich) phase when cooled below 0.867 K. At temperatures below 1 K, the Fermi liquid ^{3}He must obey the Pauli principle and behaves much the same as conduction electrons in a metal. In contrast, below 2 K the Bose liquid ^{4}He undergoes partial condensation to the superfluid state, behaving analogously to Cooper pairs in a conventional superconductor. The ^{3}He rich phase has a lower density and will float on top of the ^{3}He dilute phase. In the limit T $\rightarrow$ 0, the ^{3}He rich phase becomes pure, but the ^{3}He dilute phase will retain a constant ^{3}He concentration of 6.6%. This finite solubility of ^{3}He in ^{4}He allows for cooling power to be harnessed to near absolute zero temperature.
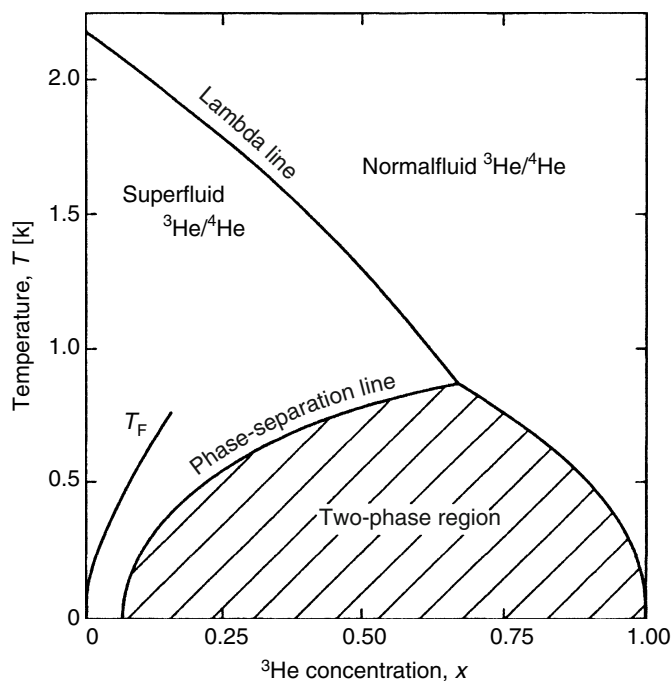
Figure 2.4: Liquid ^{3}He - ^{4}He phase diagram below 2 K [2].

For cooling to occur, ^{3}He from the concentrated phase is transported across the phase boundary into the dilute phase. In practice this is achieved by pumping on the dilute side to reach a temperature of ~ 700 mK, where the vapour pressure of ^{3}He is 1000 times larger than that of ^{4}He. This draws predominantly ^{3}He out of the dilute phase, causing the dilute phase to be out of its desired equilibrium value of 6.6%. This forces ^{3}He to cross the phase boundary and enter the dilute phase to restore equilibrium. Crossing the phase boundary results in a positive entropy change. For this to occur, energy must be absorbed from the environment, which leads to an overall decrease in temperature of the system.

2.3.2 Cooling Power of the Dilution Refrigerator

The dilution process was first proposed by Heinz London in the early 1960s [16]. In 1965, the first DR was constructed and experimentally tested, reaching a temperature of

0.22 K [17]. The cooling power of the dilution process can be derived by considering the thermodynamics of ^{3}He in the two phases. Atoms of ^{3}He crossing the phase boundary from the concentrated phase to the dilute phase is analogous to a phase change. In phase equilibrium, the chemical potentials of the two phases are equal

$$\mu_C = \mu_D \tag{2.3}$$

Recalling the definition of the chemical potential

$$\mu = H - TS \tag{2.4}$$

where H, S are the enthalpy and entropy per mole of the phase, respectively. To simplify things, assume the temperature and pressure in the two phases are equal. The equilibrium condition can then be written as

$$H_C - TS_C = H_D - TS_D \tag{2.5}$$

The enthalpy difference as a result of mixing can be written as

$$H_C - H_D = TS_C - TS_D \tag{2.6}$$

The entropy in each phase can be calculated from the heat capacity. The entropy can be obtained from

$$\int dS = \int \frac{dQ}{T} \tag{2.7}$$

Neglecting any volume change of the liquid, conservation of energy requires $dQ = dU$. Thus, the entropy is given by

$$S = \int \frac{dQ}{T} = \int \frac{dU}{T} = \int \frac{C}{T} dT \tag{2.8}$$

For the concentrated (liquid ^{3}He) phase, heat capacity measurements below 40 mK and at saturated vapour pressure give a heat capacity of $C_C = 22T$ $[J/mol\ K]$. Thus, the entropy of the concentrated phase is given by

$$S_C = \int \frac{C}{T} dT = 22\ [J/mol\ K] \tag{2.9}$$

The entropy of the dilute phase could be calculated in a similar manner, however, very few measurements at a limited number of ^{3}He concentrations have been performed. Instead, the dilute phase with ^{3}He diluted by ^{4}He can be treated as a weakly interacting Fermi liquid. As an approximation, the equation for the heat capacity of a Fermi gas can be used. For temperatures less than 100 mK, the ^{3}He concentration is $\sim 6.6\%$ and the ^{3}He effective mass is $m^* = 2.45m_3$. From this, the calculated heat capacity and entropy is $C_D = S_D = 106T$ $[J/mol\ K]$. Using Eq. 2.6, the enthalpy difference of ^{3}He in the two phases is

$$H_D - H_C = T(S_C - S_D) = T(106T - 22T) = 84T^2\ [J/mol] \tag{2.10}$$

This positive change in enthalpy implies an increase in the internal energy. Thus, energy must be absorbed from the environment, resulting in cooling. The heat of mixing for a molar flow rate $\dot{n}$ of ^{3}He transferring from the concentrated phase to the dilute phase can be written as

$$\dot{Q} = \dot{n}(H_D - H_C) = 84\dot{n}_3 T^2\ [W] \tag{2.11}$$

Thus, the cooling power $\dot{Q}$ of the dilution process is proportional to the square of the temperature T of the two phases, $\dot{Q} \propto T^2$. As an example, for a ^{3}He circulation rate of 100 μmols/sec and a temperature of 100 mK, the cooling power would be 84 μW. On a DR, this dilution process occurs in the coldest part of of the fridge known as the mixing chamber.

2.3.3   Evaporative Cooling

In addition to the dilution process in the mixing chamber, evaporative cooling also plays an important role in the DR. By mechanically pumping on the vapour above the liquid, a first order phase transition from the liquid state to the gaseous state occurs. Liquid temperatures well below the normal (1 atm) boiling point can be achieved. This can be explained simply by observing that the most energetic atoms will leave the liquid first, leaving behind the less energetic atoms. This reduces the average total energy of the liquid, resulting in a reduction in temperature. In general, the cooling power for an evaporating liquid, such as liquid helium, is given by [2]

$$\dot{Q} = \dot{n}(H_{liq} - H_{vap}) = \dot{n}L \tag{2.12}$$

where $\dot{n}$ is the molar flow rate of the evaporating liquid and L is the latent heat of evaporation. For a pump with constant volume throughput, the flow rate is proportional to the vapour pressure above the liquid

$$\dot{n} \propto P_{vap}(T) \tag{2.13}$$

In general, $P_{vap} \propto e^{-L/RT}$. Putting this all together, the cooling power of an evaporating liquid can be written as

$$\dot{Q} \propto LP_{vap} \propto e^{-1/T} \tag{2.14}$$

This demonstrates a very important concept: the cooling power decreases exponentially with decreasing temperature. Thus, evaporative cooling has a limit and becomes less efficient as this limit is approached. For the two helium isotopes, this limit is about 1.3 K for ^{4}He and 0.3 K for ^{3}He.

On a wet style DR, this effect is utilized to condense the incoming ^{3}He - ^{4}He mixture. A needle valve connects the ^{4}He bath to a small reservoir. This reservoir is continuously pumped to reach a temperature of $\sim$ 1 K. This arrangement, known as the 1 K pot

condenser, is an ideal technique to condense the incoming mixture. The low temperature reached by this method reduces the required condensation pressure, which will be discussed in more detail in section 3.2.

Evaporative cooling is also utilized for both wet and dry style DRs at the liquid-gas interface on the dilute side. On a DR, this interface occurs in the upper cold stage known as the still. Once all the mixture has been condensed, the still is responsible for maintaining a high ^{3}He circulation rate. If the still is pumped very effectively to reach a temperature of $\sim$ 0.7 K, the vapour pressure of ^{3}He will be a factor of $\sim$ 1000 times greater than ^{4}He. Thus ^{3}He will be predominantly circulated which is desired for the dilution process. Circulation of ^{4}He is to be avoided as it provides no cooling power and needs to be re-condensed, contributing a parasitic heat load to the system. Film burners are commonly employed to prevent superfluid ^{4}He creep in the still. They consist of a specific tube geometry and heater above the still that redirects superfluid flow back into the still. The heater is used to bring ^{4}He below the superfluid transition (2.172 K) and prevent further creep up into the still pipe where the ^{4}He would be pumped away.

2.3.4 Physical Arrangement

To practically realize the dilution process described above, a series of thermally isolated cold stages and heat exchangers are employed. The dilution unit consists of four major components arranged such that the phase boundary forms in the mixing chamber. These components include flow impedances, heat exchangers, the still and the mixing chamber. A simplified model of a dilution unit is show in figure Fig. 2.5.
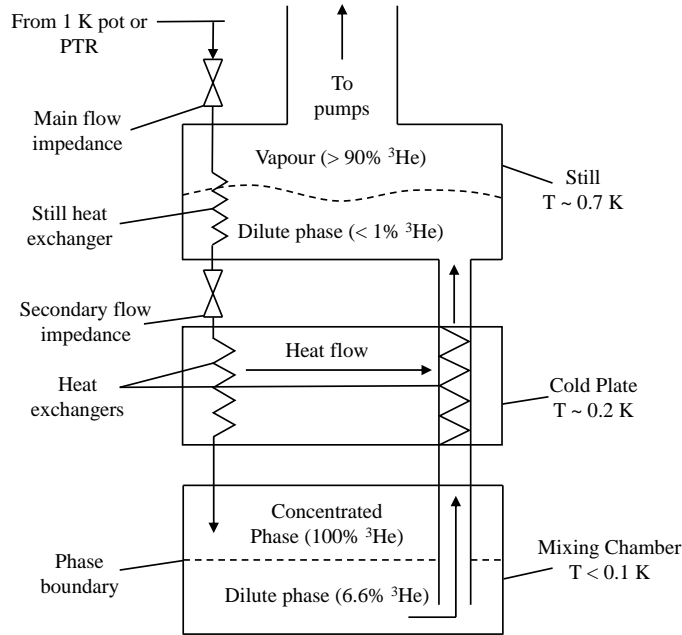
Figure 2.5: Schematic of a ^{3}He-^{4}He DR unit. Adapted from [2].

The ^{3}He-^{4}He mixture is pre-cooled by either a 1 K pot (wet style) or by a PTR (dry style) before entering the main flow impedance. The main flow impedance provides sufficient pressure build-up for condensation of the ^{3}He - ^{4}He mixture in addition to setting the nominal ^{3}He circulation rate during operation (see section 3.2). The condensed liquid then flows through a heat exchanger thermally coupled to the still. Evaporative cooling in the still cools the incoming liquid. Upon exiting the still heat exchanger, the liquid passes through a secondary flow impedance. This secondary flow impedance prevents ^{3}He from re-evaporating. Next, a series of heat exchangers are used until reaching the mixing chamber. The first heat exchanger is continuous, consisting of two concentric capillaries, which are spiralled to increase the effective surface area. Another similar design instead uses a larger capillary to house a spiralled smaller capillary as illustrated in Fig. 2.6 (a). A dilution unit with only a continuous heat exchanger can reach $\sim$ 20 mK. For temperatures less than 50 mK, the thermal Kapitza resistance ($R_K \propto (AT^3)^{-1}$) between the liquid helium and metal surface becomes very large. This resistance arises as a result of phonon mismatch

between two different media at low temperatures. As a result, heat transfer per unit area decreases rapidly with temperature. The resistance can be overcome by increasing the surface area significantly. Thus, to achieve temperatures less than 20 mK, discrete, step heat exchangers are employed. To achieve high surface area, sintered metal (e.g. silver) powder is used, as illustrated in Fig. 2.6 (b). This problem is also addressed in the mixing chamber by using sintered copper to increase the effective surface area.

(a) Concentric (continuous) heat exchanger   (b) Discrete (step) heat exchanger
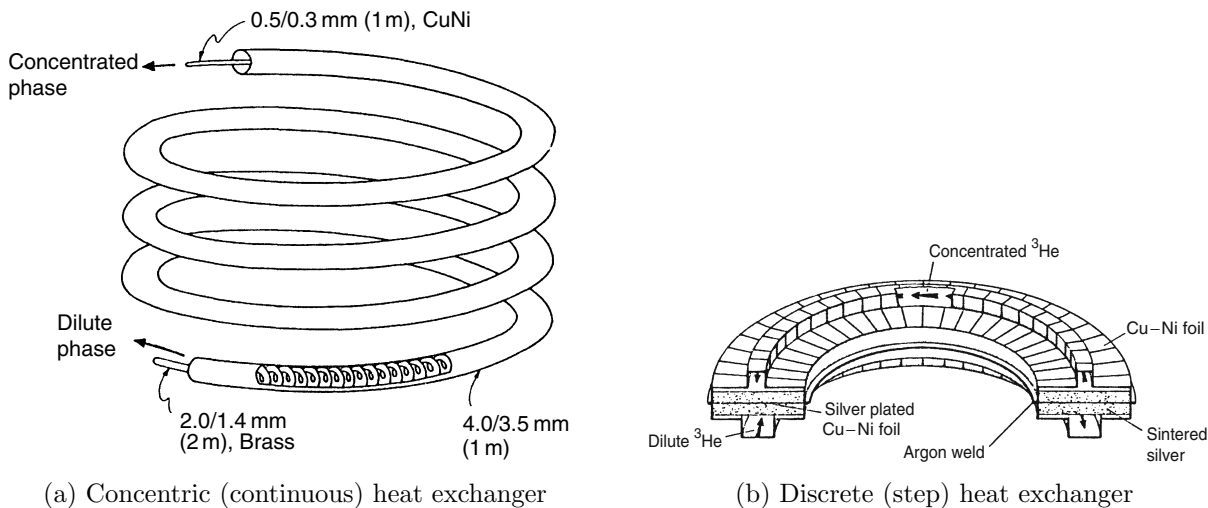
Figure 2.6: Typical heat exchangers employed in a dilution refrigerator [2].

2.4   Summary

The superior performance of PTRs in recent years has enabled a cryogen-free refrigeration method able to achieve temperatures below the boiling point of liquid helium (4 K). The ease of implementation, simplistic operation and low cost of an ADR system makes it desirable for single-shot measurements with small heat loads. In contrast, the DR has continuous and higher cooling power over the ADR. However, the DR is significantly more complicated and costly, requiring ^{3}He and several pieces of equipment to operate.

The main components needed for a DR include: a pre-cooling stage to condense the ^{3}He - ^{4}He mixture, a dilution unit (as depicted in Fig. 2.5) and a pumping system. The pumping system must be able to sufficiently circulate ^{3}He and maintain a still temperature of ~ 0.7 K. For the dilution process occurring in the mixing chamber, the cooling power is proportional to the square of the temperature $\dot{Q} \propto T^2$.

Chapter 3

Setup of Dry Dilution Refrigerator

With the theoretical basis of the DR outlined, the experimental details of modifying the cryostat will now be discussed. As mentioned previously, the Shasta model 106 cryostat was modified by replacing the ADR component with a ^{3}He -^{4}He DR. This required the design and construction of several custom components. While commercial DRs exist, the adaptation from the older wet style configuration to the modern dry configuration is still a recent development in the field. Setting up a DR in the dry configuration is more challenging as the PTR base temperature is much higher than that achieved by a 1 K pot condenser system used in a wet style DR. Kurt Uhlig, an expert in the field of ultra low temperature techniques, has authored several papers in setting up a dilution refrigerator in the dry configuration [18, 19, 20]. The modifications presented in this chapter are adapted from his previous works. The following are the key aspects of setting up the refrigerator:

- Installation of a top plate with vacuum feedthroughs on cryostat

- Design and installation of a charcoal trap and condensation stages

- Design and construction of the main flow impedance

- Implementation of a mechanical heat switch

- Design and installation of radiation baffles and pumping line

- Installation of wiring, coaxial cables and support structure to perform experiments

3.1 Condensation Stages

The condensations stages are responsible for pre-cooling the incoming ^{3}He -^{4}He mixture. For a wet style DR, pre-cooling is achieved with the ^{4}He bath and a 1 K pot condenser. In contrast, for a dry style DR, pre-cooling is achieved by heat sinking the incoming "return" line to the cold stages of the PTR. Direct PTR pre-cooling requires PTR base temperature to be sufficiently low for condensation of the mixture to occur. The heat sinking components constructed in this work were loosely based on previous designs by Kurt Uhlig [20]. In his work, circulation rates up to 1000 μmols/sec are made possible by custom clamps or direct soft soldering of the return line to the PTR 2nd stage regenerator. With this level of heat sinking, it has been demonstrated that the minimum PTR base temperature required for direct PTR pre-cooling (while also having a condensing pressure under one atmosphere) is 3.35 K. However, it has also demonstrated that this level of heat sinking is not necessary for much lower circulation rates $\leq$ 200 μmols/sec, provided the PTR base temperature is sufficiently low ($<$ 3 K). With this information, the goal was to utilize direct PTR pre-cooling to operate at a circulation rate between 100 - 200 μmols/sec with a condensation pressure of less than one atmosphere.

Illustrated in Figure 3.1, the ^{3}He - ^{4}He mixture first enters the cryostat at the 300 K plate with copper tubing, where a Klein Flansche (KF) rubber O-ring sealing flange is used. Initially for convenience, another KF sealing flange was used on the inside of the 300 K plate. However, it was determined that a KF seal on the inside of the vacuum can was inadequate due to diffusion of helium through the O-ring. This was discovered by evacuating the vacuum space at room temperature and allowing the mixture to be circulated with a pressure of $\approx$ 0.5 atm (before the main flow impedance). A mass spectrometer tuned to ^{4}He and connected to the vacuum space revealed ^{4}He to be diffusing into the vacuum space. The diffusion rate was high enough to eventually spoil the vacuum needed for the cryostat to operate. In addition, the mixture (including rare ^{3}He) would slowly be lost. Moving forward, this seal was replaced with a copper gasket seal (Swagelok, VCR fitting), much

23

return line to
diffusion & rotary pump

pressure gauge

^{3}He gas inlet

heat switch
control module

vacuum flange

copper gasket
seal

radiation shield
1st stage

charcoal trap

radiation baffle

radiation shield
2nd stage

heat switch

cold fingers

continuous counterflow
heat exchanger

step heat
exchanger

pulse tube
refrigerator
PT410

bellows

radiation baffle

PTR
1st stage
T ~ 55 K

heat exchanger
2nd regenerator

PTR
2nd stage
T ~ 2.5 K

heat exchanger
PTR 2nd stage

flow impedance
Z ~ 3.9 x 10^{11} cm^{-3}

still
T ~ 0.83 K

cold plate
T ~ 0.15 K

mixing chamber
T ~ 0.07 K

vacuum
can

Figure 3.1: Schematic of modified SHASTA model 106 Cryostat, outlining the added condensation stages, main flow impedance, radiation baffles and *Oxford* 200 dilution unit.

24

the same as used in an ultra high vacuum (UHV) environment. Next, a short section of coiled stainless steel tubing is used to connect the VCR fitting to the PTR 1st stage. Stainless steel tubing is used due to its relatively poor thermal conductivity. The coiled length reduces stress on the hard (silver) soldered (45/30/25 Ag-Cu-Zn) joints caused by thermal expansion/contraction. The gas then enters into a charcoal trap, designed to freeze out any contamination that was introduced into the mix (e.g., water, nitrogen). The positioning of the tubing for the inlet/outlet of the trap was also carefully considered, forcing the incoming gas to pass through the cold charcoal before exiting the trap. Thermalizing the gas near 60 K (PTR 1st stage) reduces the heat load on PTR 2nd stage where the cooling power is significantly lower. The trap was constructed using copper pipe that was filled with charcoal fragments. The tubing was then soft-soldered (60/40 Sn-Pb) into a copper plate and securely mounted onto the PTR 1st stage. The outlet of the trap then connects to stainless tubing coiled around the 2nd regenerator of the PTR. The tubing was wrapped tightly around the regenerator and three hose clamps were installed to hold it in place. The long coiled length of stainless steel tubing provides thermal isolation between the first and second stage of the PTR. At the outlet of this heat exchanger, the tubing switches to a small diameter (0.02" OD) copper nickel capillary. This capillary was wound around a solid, cylindrical piece of copper which is securely mounted onto the PTR 2nd stage. The CuNi capillary is soft soldered to the puck to provide a rigid, thermal connection. At the output of this heat exchanger, the gas then enters the main flow impedance (described in section 3.2) and finally the *Oxford* 200 Dilution unit.

On the output of the dilution unit, the pumping orifice for the still connects to a stainless steel pipe with an indium seal. Indium seals are ubiquitous in low temperature apparatuses for making leak-tight connections at low temperatures. They consist of a male/female flange and indium, a highly ductile substance at room temperature. The indium can be formed into an O-ring shape and compressed by a ring of fasteners. Directly above the still orifice, a radiation baffle (Fig. 3.7 (a)) was inserted into the still pipe to absorb and block radiation from irradiating the still. The still pipe was heat sunk (clamped) at the PTR 2nd stage pipe to reduce the heat load on the still in addition to providing rigidity to the system. The clamp consisted of two halves of copper with the center drilled out to a size that equalled the outer diameter (OD) of the pipe. Each half was then sanded to remove a

25

few thousandths of inch of the material (along the edge with half circle). This reduced the clamp hole size to be slightly less than the OD size of the pipe. Furthermore, high electrical conductivity silver paint was added between the joint to fill-in contact imperfections and increase the thermal conductivity at low temperatures. At the PTR 1st stage, the pipe is clamped again and fitted with another radiation baffle in the pipe. The radiation baffle is a shiny aluminum "potato chip" geometry (Fig. 3.7 (b)) used to absorb and block 300 K radiation from above. A flexible bellows is used between the PTR 1st stage and the 300 K plate to reduce stress on components due to thermal expansion/contraction.

3.2   Main Flow Impedance

A key component in all DRs is the main flow impedance. As mentioned previously, the main flow impedance is located on the input line to the dilution unit and provides sufficient pressure for the ^{3}He - ^{4}He mixture to condense. The PTR pre-cools the incoming mixture to that of the PTR 2nd stage $\sim$ 2.5 K. However, in order for ^{4}He (^{3}He) to undergo a phase transition to a liquid state at this temperature, a pressure of 106mbar (453mbar) is required. Without this impedance, no condensation of the mixture would occur. This impedance also sets the nominal circulation rate, typically reported in μmoles/sec, of ^{3}He after all the mixture has been condensed.

For wet style DRs, a 1 K pot condenser pre-cools the incoming mixture to $\sim$ 1 K, as described previously. At 1 K, the condensation pressure required for ^{4}He (^{3}He) is 0.13mbar (12mbar). A 1 K pot condenser significantly reduces the condensation pressures required, when compared to PTR pre-cooling. Since the main flow impedance for the *Oxford* 200 dilution unit was designed for a 1 K pot condenser, it needed to be replaced with one of much higher value ($Z_{PTR} \gg Z_{1K\ POT}$).

The construction of the new impedance was very simple: insertion of a wire into a capillary with a slightly larger ID than the wire. A few centimeters of steel piano wire ($0.009''$ OD) were inserted into a CuNi capillary ($0.010''$ ID). To measure the impedance after it was constructed, the capillary was soft soldered to a *Swagelok* fitting and connected to a nitrogen gas cylinder. The gas cylinder was regulated to provide an output pressure of

Table 3.1: Table I. Characteristics of refrigerator for three different impedances Z. [21]

Impedance	Z=2.00x10^{12}cm^{-3}	Z=1.26x10^{12}cm^{-3}	Z=0.67x10^{12}cm^{-3}
Unfilled quasi-equilibrium T (K)	1.17	1.18	1.26
Equilibrium T (K)	1.26	1.27	1.33
Flow (moles/sec)	1.85x10^{-4}	2.4x10^{-4}	3.3x10^{-4}
Critical power (mW)	8.2	10.7	15
Time for filling (min)	9	5	2.2
$\dot{Q}/\dot{n}$ (mW/10^{-4} moles/sec)	4.4	4.5	4.5
Flow x Z (10^{-4}moles/sec x 10^{12}cm^{-3})	3.7	3.0	2.2

3-5 psi, allowing gas to trickle through the impedance. A graduated cylinder was filled with water and inverted into a bowl, which was also filled with water. A retort stand was used to keep the inverted graduated cylinder submerged in the bowl of water. The impedance was placed in the bowl of water and positioned under the inverted graduated cylinder. Nitrogen gas ($\eta = 18$ μPa·sec) flowing through the impedance was allowed to enter the graduated cylinder, displacing water from it. From this displacement, a measurement of volume as a function of time can be made, utilizing the gradations on the cylinder. The graduated cylinder was kept short (< 10 cm) to ensure the pressure at the top of cylinder is maintained near one atmosphere. DeLong *et al.* [21] used a similar technique and calculated the value of the impedance using the following relation

$$Z = (1/\eta)\Delta P/\dot{V} \tag{3.1}$$

Where ΔP is the pressure drop that generates a volumetric flow $\dot{V}$ for a gas with viscosity coefficient η. DeLong *et al.* also provided an estimate for the desired value of the impedance, providing a table of empirical data for impedances and the corresponding flow rate in μmoles/sec for continuously circulating ^{4}He (Table 3.1).

Several impedances were constructed and their impedance values measured. Impedances with a value of 1-5 x 10^{12} cm^{-3} were installed in the cryostat first, following the table

provided by Delong *et al.* Testing these impedances while cold resulted in cooling of the mixing chamber to ~ 1 K, indicating condensation of ^{4}He. However, the measured circulation rate was too low (< 10 μmoles/sec) for liquid ^{4}He to stay condensed in the cryostat. Nevertheless, the table provided a good starting point. Moving forward, impedances were made with a value an order of magnitude lower 1-5 x 10^{11} cm^{-3}. Finally, an impedance with a value of 3.9 x 10^{11} cm^{-3} was installed and was able to condense all the ^{3}He - ^{4}He mixture with a circulation rate between 100 - 150 μmoles/sec. This was the final and current impedance used in the cryostat.
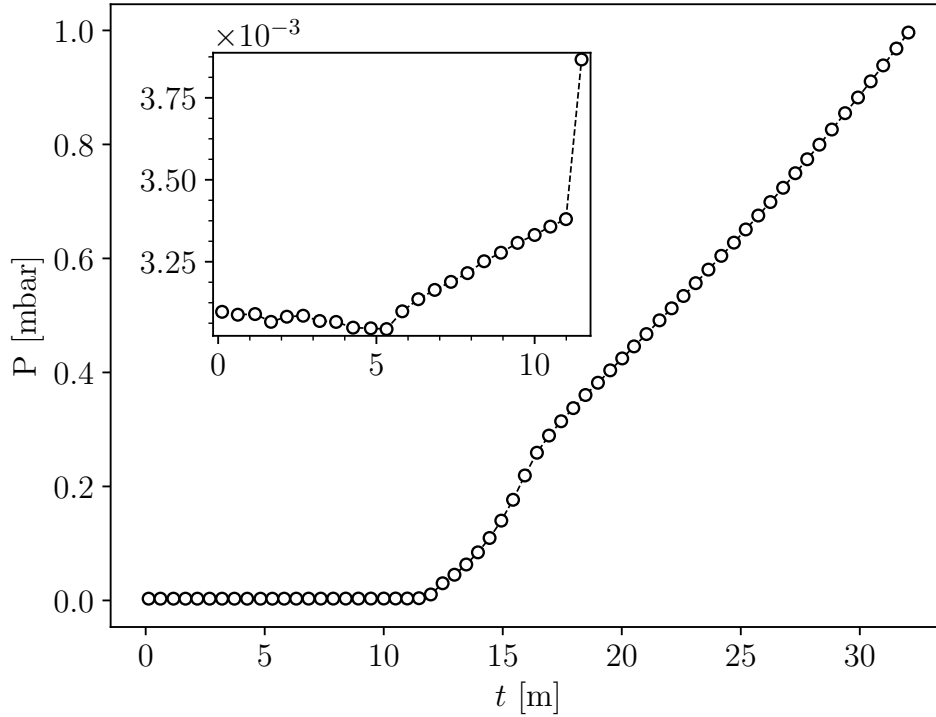
Figure 3.2: Main flow impedance testing at room temperature. The impedance with value of 3.9 x 10^{11} cm^{-3} was installed in the cryostat and a flow test was performed.

The impedance was installed on the cryostat with two soft solder joints. In the future, an indium seal could be installed to conveniently replace the impedance. Leak checking was performed by using a mass spectrometer tuned to ^{4}He. The soft-solder joints for installing

the impedance are very technically challenging. If heat is applied for too long, solder can easily wick into the impedance. To check if the impedance had blocked during installation, a flow test at room temperature was performed. The room temperature flow test measured the pressure build up in the still pipe (in the cryostat) as a result of allowing ^{3}He - ^{4}He mix to be pressurized to ~ 0.5 atm before the main flow impedance. A pressure gauge at the top of the cryostat (see Fig. 3.1) was used along with a manual valve located immediately after this gauge. Since the flow impedance value is very large, it was important to first measure the out-gassing rate. Out-gassing occurs in all vacuum systems and is a result of gas sources (such as moisture) being absorbed and trapped on surfaces. Before adding mix, the still (pipe and pumping line) were thoroughly pumped (1-2 days) to achieve a good vacuum (~ 3 μbar). At the ~ 5 minute mark (see inset of Fig. 3.2) of this test, the valve at the top of the cryostat was closed which forces gas (from out-gassing) to collect in the still pipe. The out-gassing rate was measured for ~ 5 minutes. At the ~ 12 minute mark, mix was added to pressurize the main flow impedance and a sharp increase in pressure was observed (Fig. 3.2). As a useful metric for future impedances and/or to evaluate the installed impedance over several cool-downs, the test was continued until a pressure of 1 mbar was reached (~ 20 min for this impedance).

3.3   Heat Switch

The dilution unit is very poorly thermally linked to the PTR 2nd stage, connected only by the stainless steel still pipe and the main flow impedance (negligible thermal conductance). This high thermal resistance is ideal during operation, however, a problem arises of how to initially cool the dilution unit to the temperature of the PTR 2nd stage. For wet style DRs, the liquid helium bath encompasses the vacuum can surrounding the dilution unit. During the cool down process, a small amount of exchange gas (typically ^{4}He) is added to the vacuum space containing the dilution unit. The ^{4}He gas provides a thermal link between the bath and the dilution unit. Once the dilution unit reaches thermal equilibrium with the bath, the exchange gas is pumped away and the ^{3}He - ^{4}He mixture is circulated.

For the Shasta cryostat, there is only a single vacuum space separating room temper-

ature from the PTR (1st and 2nd stage) and the dilution unit. This arrangement is very convenient as it eliminates indium seals and vacuum feed-throughs for a secondary, low temperature vacuum space. However, it also means that exchange gas cannot be added to the vacuum space as this would also thermally link the PTR stages to the room temperature outer vacuum can. Instead of exchange gas, other low temperature switch options include a mechanical switch, a superconducting switch or a hermetically sealed tube filled with exchange gas. The mechanical switch functions by thermally disconnecting the two cold stages, requiring a vacuum feed-through that supports physical movement. A superconducting switch takes advantages of the thermal resistance of the superconducting state. It functions by using a superconducting material to connect the two cold stages. Once the material reaches the critical temperature T_c, electrons begin to condense into Cooper pairs exponentially with decreasing temperature, of which are unable to transport heat. The hermetic tube with exchange gas functions similarly, allowing heat transfer between the two stages until the exchange gas condenses/freezes out.

For this system, a mechanical switch was employed to thermally link the still and mixing chamber (independently) to the PTR 2nd stage by machined copper "fingers". The switch and fingers are illustrated in Fig. 3.1. The switch employs a stepper motor at room temperature and a rotating vacuum feed-through. The switch and feed-through came with the cryostat and was used previously for the ADR system to thermally connect/disconnect the salts to the PTR 2nd stage during magnetization/demagnetization cycles.

3.4 Thermometry

An obvious aspect of any low temperature cryostat is knowing the temperatures of the various stages. Thermometers are classified as either primary or secondary. Primary thermometers map the raw physical quantity being measured to a temperature, requiring understanding of the physical mechanism. An example of a low temperature primary thermometer is the angular anisotropy of gamma rays emitted by certain radioactive nuclei. In contrast, the measured quantity in secondary thermometers has no direct temperature correlation, instead requiring calibration from a primary thermometer. Resistance

thermometry is a secondary thermometer which uses the temperature dependence of the electrical resistance of certain metals or semiconductors. It is most commonly used due to its ease of implementation, sensitivity (Ω/K) and repeatability. However, for temperatures below 50 mK, resistive thermometry becomes very challenging due to noise pickup and increased thermal (Kapitza) resistance. These effects result in self heating of the thermometer, causing it to read incorrectly. Luckily, the cryostat in this work was limited to a base temperature of 70 mK and employed diode (secondary) and resistance (secondary) thermometers to measure the several cold stages.

For the PTR, silicon diodes (*LakeShore*, model DT-670) are used with one mounted on each PTR stage. Diode thermometry is based on the temperature dependence of the forward voltage drop in a p-n junction biased at a constant current. A current supply supplies a constant current of 10 μA and the corresponding voltage drop is measured using the analog inputs of a lockin amplifier (Stanford research systems, model 830). To optimize the PTR base temperature (2nd stage) it was important to have an accurate and reproducible thermometer on this stage. Thus, temperature response data obtained from *LakeShore* was fitted to a least squares 10th order polynomial. Two fits were performed in order to prioritize the change in response dV/dT that occurs at $\sim$ 25 K. Fig. 3.3 shows the fit to the temperature response data.

For the dilution unit, resistance thermometry was employed. The electrical resistance measurement utilizes an AC resistance bridge (Lake Shore, Model 370). The four wire AC (13.7 Hz) measurement eliminates lead resistance and reduces the effect of lead capacitance in the measurement. To reduce high frequency noise pickup, commercial π filters (inline inductor with two capacitors to ground on either side) are employed on all electrical feedthroughs of the cryostat. Additionally, twisted pair wiring is used throughout the cryostat to further reduce noise pickup. The main thermometer used for the experimental cold stage (thermally linked to the mixing chamber) is a commercial *LakeShore* germanium resistance thermometer (GRT). This thermometer comes with a calibration and has already been thermally cycled several times for excellent reproducibility. An additional (previously calibrated) ruthenium oxide (RuO_2) resistance thermometer was placed in direct contact (strong thermal link) with the mixing chamber. This thermometer was useful in monitoring the thermal link between the mixing chamber and the experimental cold stage. Two other
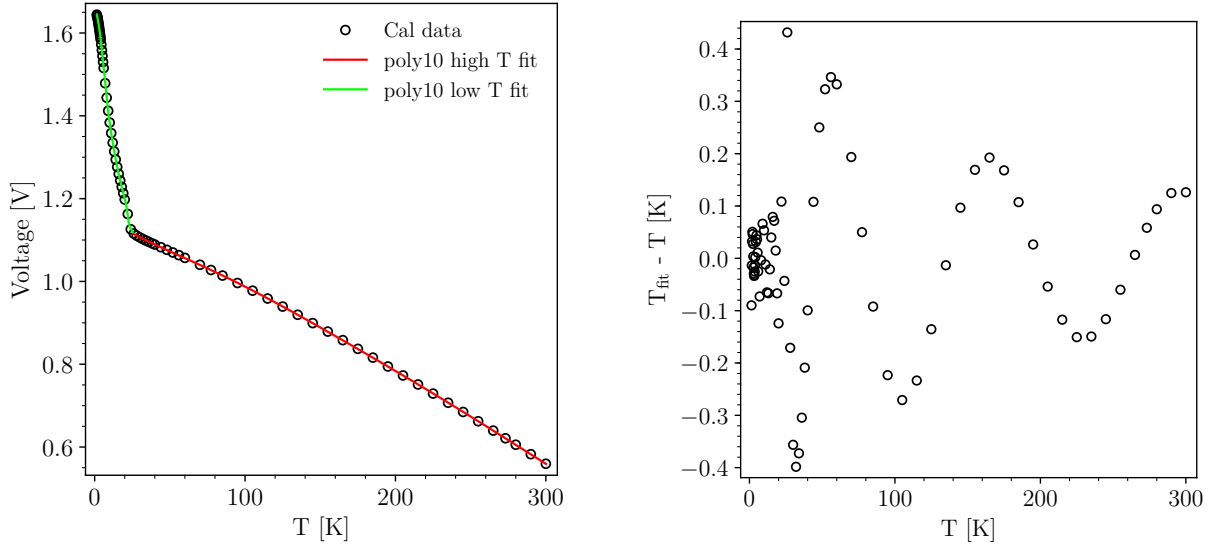
(a) High and low temperature fits to calibration
data provided by *LakeShore*.

(b) Residual of fit.

Figure 3.3: PTR diode thermometers, fit and residual.

carbon glass resistance thermometers were calibrated in reference to the RuO_2 thermometer on the mixing chamber. Carbon glass thermometers are convenient as they are easily sourced, inexpensive and follow a near exponential form with no higher order derivatives. The carbon glass thermometers were fit to an empirical relation that was first proposed by Clement and Quinnel [22]

$$\ln R + \frac{C}{\ln R} = A + \frac{B}{T} \tag{3.2}$$

The result of the fit is shown in Fig. 3.4, which has a corresponding residual of less than 40 mK over the temperature range of 100 mK to 4.2 K. These thermometers were mounted on the still and intermediate cold plate on the dilution unit and provided useful information for getting the DR operational.
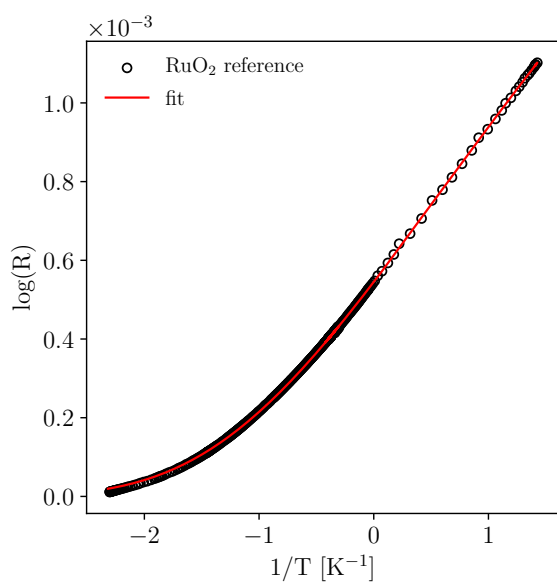
(a) Empirical fit, using calibrated RuO$_2$ reference data.
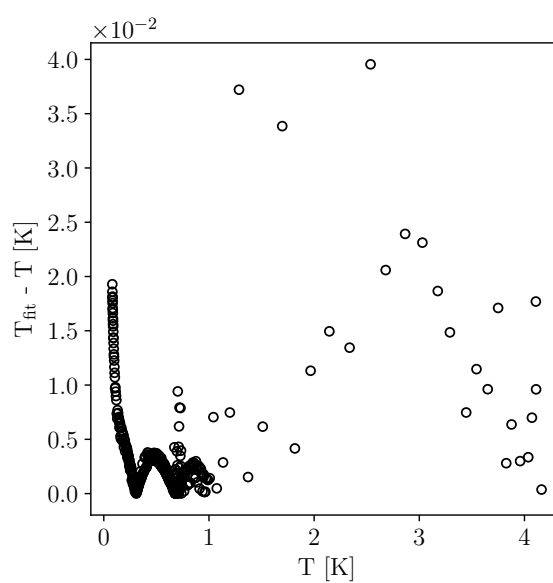
(b) Residual of fit.

Figure 3.4: Carbon glass resistance thermometers, fit and residual.

3.5 Pumping System

In order to circulate the mixture, a series of pumps along with a gas handling system (GHS) is used. A schematic of the GHS is shown in Fig. 3.5. This was the GHS for the *Oxford* 200 DR, used in the wet configuration. Several features involving the 1 K pot condenser were omitted while running in the dry configuration. The role of the GHS is to store, condense, circulate, clean and pump the ^{3}He - ^{4}He mixture. An important design aspect of the GHS is to keep the pressure of the mixture under one atmosphere at all times. This safety feature ensures that the mixture is never lost due to a leak in the system. If the system is always under partial vacuum (i.e., under one atm) and a leak in the system were to occur, air would leak into the system but the mixture (including rare ^{3}He) would not be lost. The mixture is stored in a large, sealed storage container ("dump") with enough volume such that the pressure is maintained under one atm. The mixture is cleaned from any contamination with cold traps (CT1, CT2) which consist of charcoal filters submersed in liquid nitrogen at 77 K. Contamination of the the mixture can occur from a small leak in the system and/or chemical decomposition of the oil used in the pumps.

The pumps used for circulation are located inside the GHS, which was designed to be a portable unit. The pumping system consists of a rotary vane pump (Alcatel, model #402723) and an oil vapour booster pump or diffusion pump (Edwards, model 9B3). A rotary pump consists of variable length vanes connected to a rotor. The rotor rotates inside a circular cavity creating multiple chambers for which the gas is drawn in, mechanically compressed by the vanes and exhausted. In this system, the inlet of the rotary pump is connected to the outlet of the diffusion pump. Diffusion pumps can achieve superior vacuum over mechanical positive displacement pumps, like a rotary pump. For this system, a diffusion pump is able to provide very low inlet pressures and thus a low vapour pressure in the still. The diffusion pump operates by heating a reservoir of a hydrocarbon oil until it vaporizes. This vaporized oil is forced out through a series of fine nozzles, which are directed partially downwards (toward the pump outlet) and to the outer walls of the pump. The outer walls of the pump are water cooled to re-condense the oil and return it to the heater reservoir. The supersonic oil vapour from the jets can collide and transfer momentum to gas particles. This results in a net increase in pressure towards the base of
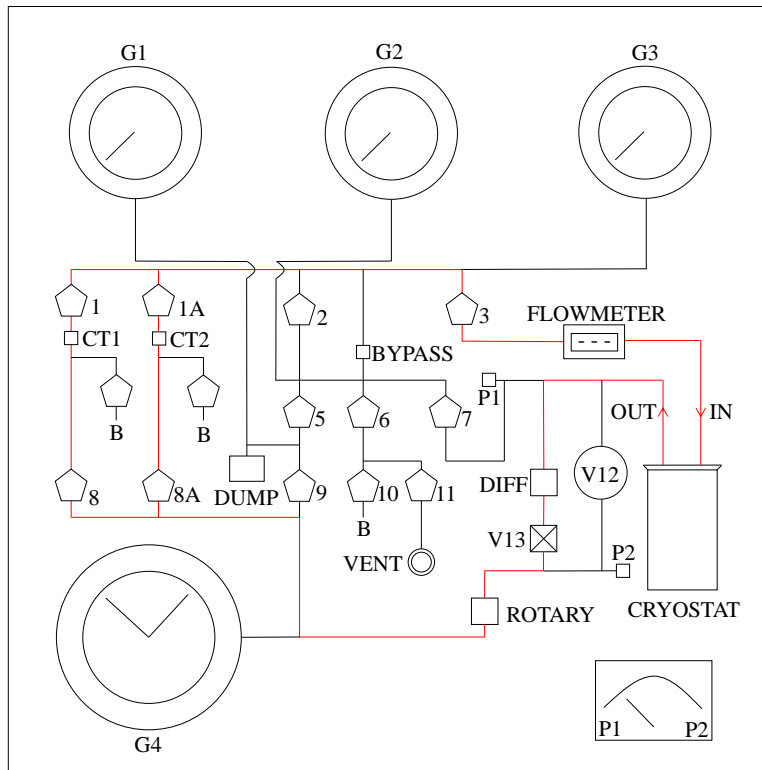
Figure 3.5: Schematic of the top half of gas handling system (GHS) used to operate the DR. The red line indicates the ^{3}He flow path during operation. Other sections of the GHS not used for the dry operation have been omitted.

the pump, where the gas is collected by the rotary pump. A schematic of the two pumps are illustrated in Fig. 3.6.

(a) Rotary vane pump

(b) Oil vapour booster (diffusion) pump
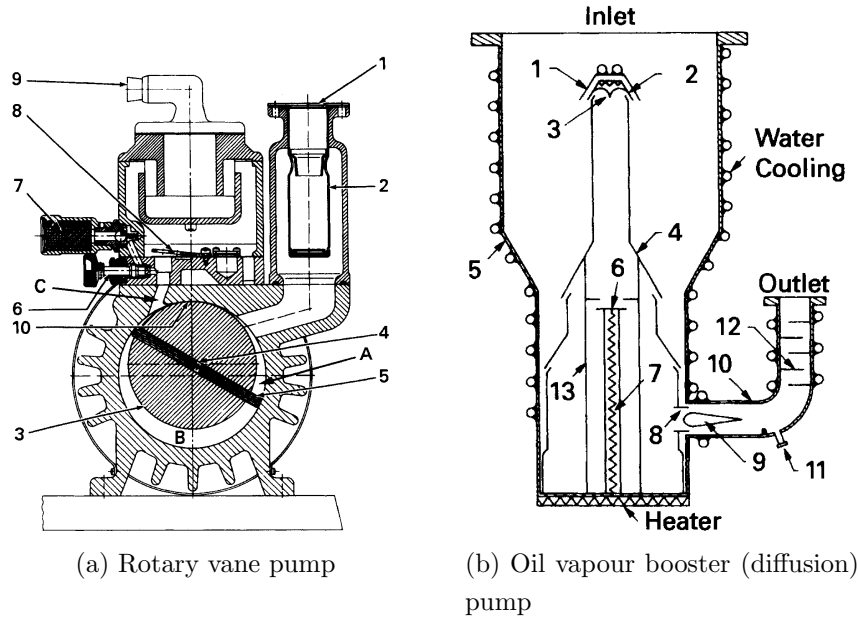
Figure 3.6: Schematic of the pumps used for the pumping system in this work [3].

3.6 Heat Load Considerations

3.6.1 Heat Transfer Mechanisms

Critical to the design of all cryostats is the ability to quantify the heat load between the various cold stages. For heat transfer calculations, it is convenient to use the upper limit to estimate the order of magnitude of heat load. In general, heat transfer can propagate by three different mechanisms: conduction, convection and radiation. Cryostats operate under vacuum and thus convection does not exist. Conduction heat load occurs from structural supports, piping, and wiring within the cryostat. The heat transfer by conduction is given by Fourier's law

$$\dot{Q} = \kappa \nabla T \tag{3.3}$$

where $\dot{Q}$ describes the heat flux (Wm^{-2}) through material of thermal conductivity κ and

temperature gradient ∇T. Heat transfer by conduction can be reduced by choosing materials with a low thermal conductivity κ and small cross-sectional area. Electromagnetic radiation is emitted from all surfaces that are at finite temperatures. The radiation heat flux (Wm^{-2}) emitted from a black-body surface at temperature T is given by the Stefan-Boltzman law

$$P = \sigma T^4 \tag{3.4}$$

where σ is the Stefan-Boltzman constant. Very few surfaces behave as blackbodies but instead have a material dependent property known as emissivity ϵ. Emissivity can be no greater than unity and is also wavelength dependant. Thus, it is usually desirable to incorporate reflective surfaces that have a low emissivity/absorptivity to incident radiation.

3.6.2   Radiation Considerations

The Shasta cryostat came equipped with radiation shields for both stages of the PTR. Our group had previously added reflective superinsulation to the outside of each of the shields in an effort to reduce radiation heat load on PTR stages. The innermost shield connected to the 2nd stage PTR has a black coating on the inside. This coating is to immediately absorb any leaked radiation from higher temperature stages.

The dilution unit is housed inside the innermost radiation shield which is thermally linked to the PTR 2nd stage. This shields radiates $\sim$ 2.5 K radiation onto the dilution unit. A rough calculation was performed to determine if this radiation could spoil the base temperature of the cryostat. The physical geometry of the mixing chamber can be considered to be a cylindrical "puck", with a height of 5 cm and radius of 4 cm. Thus, an estimate of the outer surface area of this mixing chamber is $\sim$ 0.023 m^2. To further simplify the problem, the surface of the mixing chamber can be assumed to behave as an ideal black-body surface ($\epsilon = 1$). The heat transfer between the radiation shield and mixing chamber is given by the difference between radiation emitted from the shield and absorbed by the mixing chamber and radiation emitted by the mixing chamber and absorbed by the

shield

$$\dot{Q} = \sigma(T_{shield}^4 - T_{M.C.}^4)A_{M.C.}F \tag{3.5}$$

where $A_{M.C.}$ is the surface area of the mixing chamber and F is a geometric view factor [23] that accounts for the relative orientations of the two surfaces. In the limit of thermal equilibrium (i.e., $T_{shield} = T_{M.C}$) the heat transfer is zero. The value of F is between zero and one and can be difficult to compute for irregular geometries. Thus, only the case of maximum heat load (i.e., $F = 1$) will be considered. The maximum heat transfer between the bodies occurs for when $T_{M.C} \rightarrow 0$. Assuming the shield temperature is 2.5 K, an upper limit for the heat load on the mixing chamber is ~ 0.05 μW. If the shield temperature was slightly higher at 5 K (due to radiation from the 60 K shield) the heat load would be ~ 0.8 μW. While not completely insignificant, heat loads of one μW and less can be regarded as small. Since this calculation is an upper limit, the heat load was regarded as insignificant. However, this is only true if the PTR 2nd stage shield temperature is at or near the PTR 2nd stage temperature. To experimentally confirm that this is true, a radiation shield thermally connected to the still could be placed around the dilution unit, reducing the radiation power on the mixing chamber by a factor of ~ 160.

Another radiation concern was on the inside of the still, caused by 300 K and/or 60 K radiation travelling down the inside of the still pipe (inside the cryostat). It is again useful to assume the worst case scenario, where the bellows at the top of the cryostat (300 K) and the inside surface of the still (0.7 K, 0.5" diameter still orifice) both behave like ideal blackbodies ($\epsilon = 1$). Using equation 3.5, the maximum heat load for 300 K radiation would be ~ 58 mW. For 60 K radiation the maximum heat load would be ~ 0.09 mW. For a still operating ideally, applied heat values to circulate faster are in the range 10 - 20 mW. Thus, over 50 mW of heat would overload the still while 0.09 mW would provide a minor, intrinsic heat load.

When first setting up the cryostat, the goal was to have as little radiation heat load through the still pipe as possible. If the heat load was too high, the still could heat up and prevent condensation of the incoming mixture. Thus, two separate radiation baffles were installed inside the still pipe, located at each of the PTR stages. The baffle at the PTR 1st

38
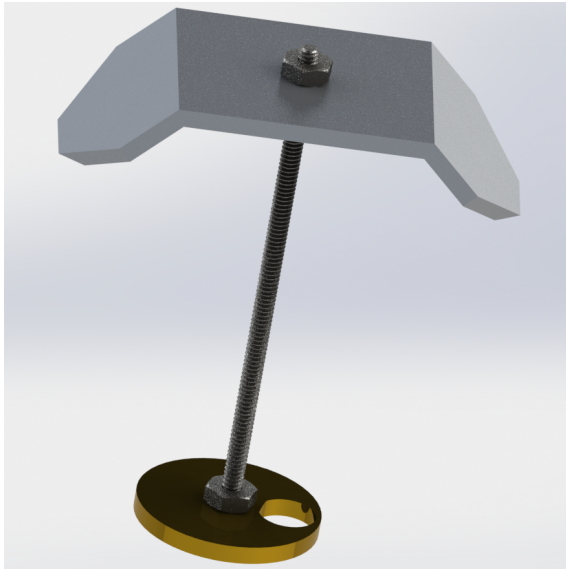
(a) Upper radiation baffle.
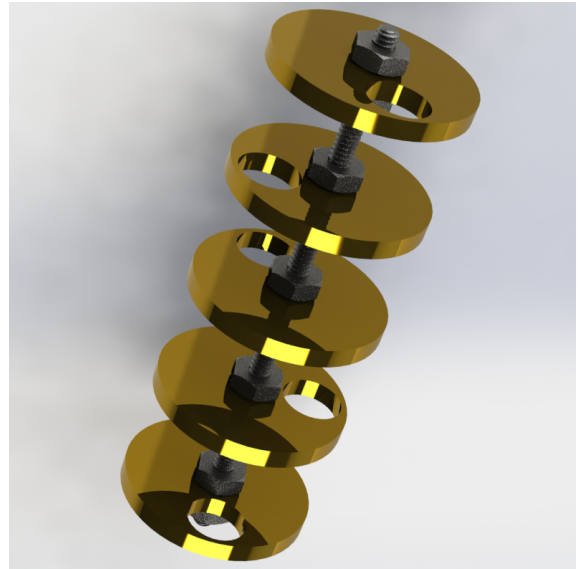
(b) Lower radiation baffle.

Figure 3.7: Radiation baffles inserted into the still pipe to block 300 and 60 K radiation from entering the still.

stage consists of a polished aluminum plate, bent into a "potato chip" shape. The plate rests on the the bottom of the bellows, near clamp to the PTR 1st stage. A 4-40 threaded rod connects the aluminum plate to another circular plate made of polished brass. Situated inside the still pipe, this plate is drilled away on one side to allow gas flow. Its function is to provide additional radiation isolation while also centering and stabilizing the upper aluminum plate. The second radiation baffle is located just above the still and consists of five of these circular brass plates in series. By placing multiple plates in series, the net flux of radiation reaching each baffle is reduced. If the thermal link from the plates to the still pipe is not too weak, the lower plates of this radiation baffle will be approximately equal to the temperature of the still pipe (~ 2.5 K) that they are in contact with. This results in an acceptable amount (~ 2.5 K) of radiation entering the still. However, this lower radiation baffle was later removed as it was suspected that it was providing too much flow impedance. With the baffle, the still temperature was ~ 0.83 K. In the next cool-down with the baffle removed, the still temperature dropped to a more ideal value of ~ 0.73 K.

3.7 Operation and Performance

3.7.1 Operation

The operation of the cryostat is unique due to the custom configuration. To prepare cooling down, the dilution unit, components connecting to the GHS and cold traps must be thoroughly evacuated such to remove any air/contamination in the system. Next, radiation shields are securely fastened to each of the PTR stages. The vacuum can is then lifted by a counter-weight pulley system and clamped to the 300 K plate. Finally, the vacuum space is evacuated to a pressure less than 65 mbar and the PTR compressor is turned on. During cooling, the heat switch should be in the closed position (i.e., connecting the PTR 2nd stage to the still/mixing chamber). The system takes $\sim$ 36 hours (Fig. 3.8 (a)) to fully reach the base temperature of the PTR 2nd stage $\sim$ 2.5 K.

While the PTR is cooling the system, the GHS can be turned on. This includes turning on the main rotary pump and the oil vapour booster pump. The booster pump must be allowed to warm up ($\sim$ 1 hour) before opening the pneumatic gate valve connected to the still pumping line. A dewar can be filled with liquid nitrogen and one cold trap can be placed in the dewar. Once the dilution unit has reached base temperature of the PTR 2nd stage, the heat switch can be opened. The mixture from the storage container can be allowed to enter the cold trap and can then throttled into the cryostat using valve 3 (see Fig. 3.5), monitoring the flow meter as to not exceed 200 μmoles/sec. After $\sim$ 30 min, the valves can be fully opened. Once the pressure in the storage container reaches $\sim$ 600 mbar, the mix must then be "stuffed" into the back of the diffusion pump in order to maintain a high condensation pressure. This is achieved by closing valve 9 and throttling valve 7 (see Fig. 3.5) such that the pressure does not get too high ($<$ 0.1 mbar) at the inlet of the diffusion pump. It takes $\sim$ 24 hours for all the mixture to condense, slowly opening valve 7 every couple of hours. Once all the mixture has been condensed, it is crucial that valves 5 and 7 be left fully open in the event the pumps shut off (i.e., from a power outage) such that the mixture can slowly collect in the storage container.

To warm up the cryostat, the mixture must first be re-collected back into the storage container. Valves 8, 8A, 3, 5, and 7 can be closed and valve 9 can be opened. This will stop
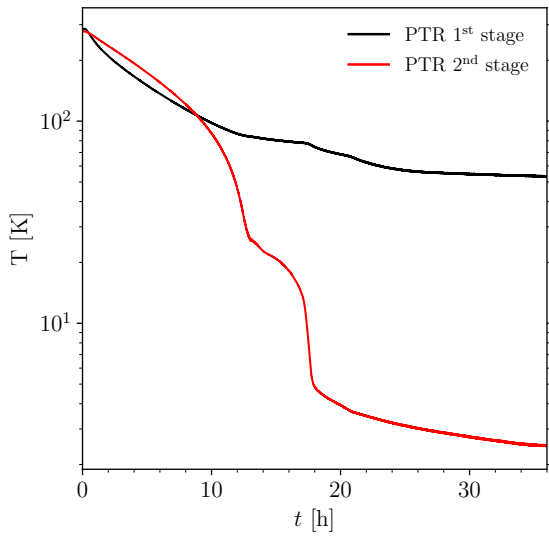
(a) PTR stages cooling.
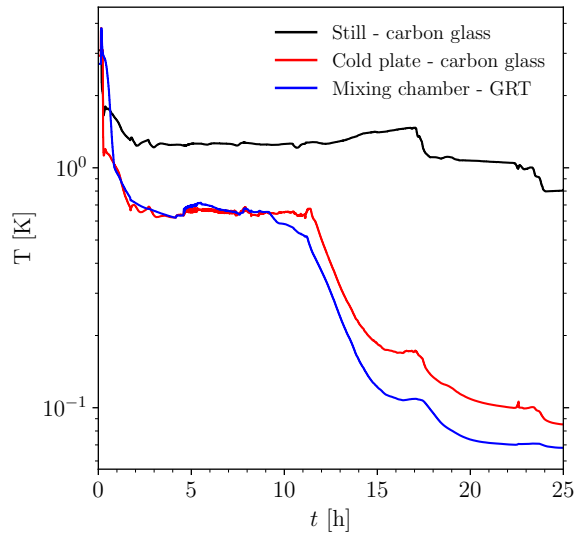
(b) Adding ^{3}He - ^{4}He mixture. Still, cold plate and mixing chamber cooling.

Figure 3.8: Typical cool-down data for various stages of the cryostat. With the heat switch closed and connected to the dilution unit, the entire system cools to 2.5 K in $\sim$ 36 hours. The mixture can then be added which requires $\sim$ 24 hours to fully condense. Overall the cryostat can cool down fully in 60 hours and warm up within the same amount of time.

circulating ^{3}He back into the cryostat and begin collecting the mixture into the storage container. To accelerate the process, heat can be applied to both the still and mixing chamber. Once all of the mixture has been collected, the pneumatic gate valve (V13 in Fig. 3.5) can be closed to stop pumping on the still. The heat switch can be closed and the PTR compressor shut off. A small amount of ^{4}He exchange gas can be added to the vacuum space to further decrease the time to warm-up.

3.7.2 Performance

The performance of the DR was evaluated with a few simple metrics. The base temperature of $\sim$ 70 mK was measured with a calibrated GRT thermometer on the mixing chamber. To characterize the cooling power of the DR, the partial-integral-derivative (PID) controller of the *Lakeshore* resistance bridge was set to a target temperature for the RuO$_2$ thermometer located on the mixing chamber. The temperature is controlled using a resistive heater (500 Ω), also located on the mixing chamber, to supply known amounts of heat. This test is commonly used by manufactures and in literature as a performance metric. This process was automated to step the temperature from base temperature 70 mK to 125 mK in 5 mK increments. For each data point, a time of one hour was waited for the system (and heater power) to stabilize. Data was collected with no still heat in addition to the maximum amount of still heat for stable operation (0.35 mW). Unfortunately, the still performance during this cool-down was not ideal, allowing only a small amount of still heat to be applied (little contrast to no still heat). The results are plotted in figure 3.9 (a). A plot of applied heat $\dot{Q}$ as a function of temperature squared T^2 (Fig. 3.9 (b)) gives the expected cooling power of a DR. Extrapolation of the y-intercept for no still heat (23 μW) and with still heat (23.9 μW) provides an estimate of the intrinsic heat load on the mixing chamber at base temperature. With still heat, the intrinsic heat load is higher as a result of an increased circulation rate. The poor base temperature is a direct result of an intrinsic heat load of $\sim$ 23 μW of heat on the mixing chamber.
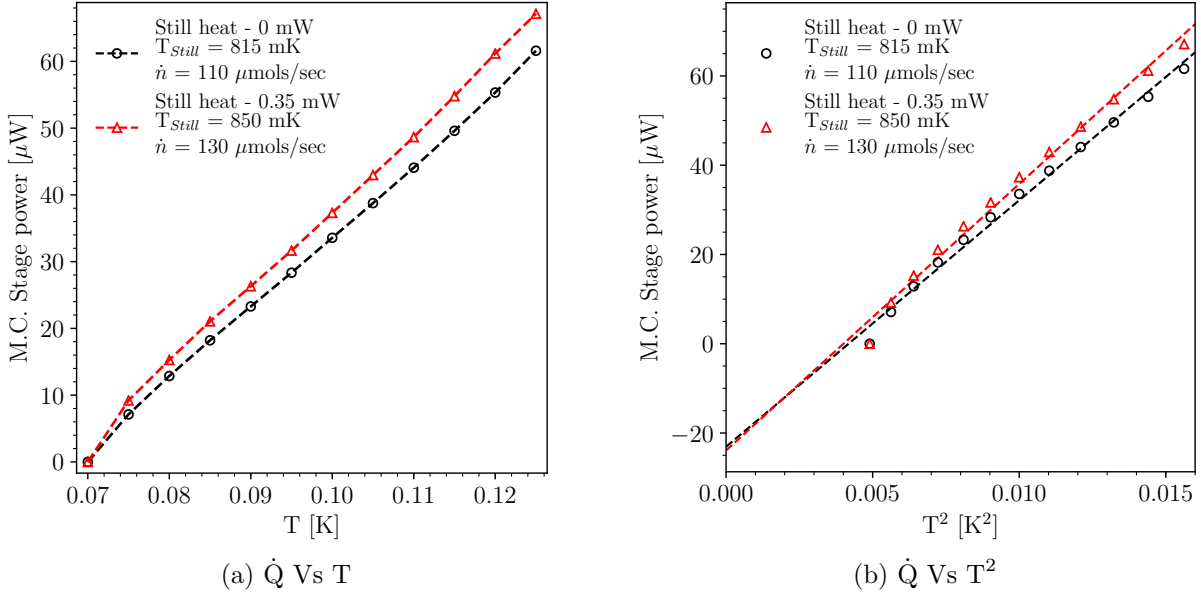
Figure 3.9: (a) Mixing chamber heater power as a function of temperature. (b) Mixing chamber heater power as a function of temperature squared, the expected cooling power for a DR. The circulation rate began increasing for higher mixing chamber heater powers.

Table 3.2: DR Operating Specifications.

$\dot{Q}_{\text{still}}$ (mW)	$\dot{Q}_{\text{M.C.}}$ (μW)	$\dot{n}$ (μmols/sec)	Condensing Pressure (mbar)	PTR 1st Stage (K)	PTR 2nd Stage (K)	Still (mK)	Cold Plate (mK)	Mixing Chamber (mK)
0	0	110	675	57	2.45	815	84	70.0
0.35	0	130	840	58	2.47	850	110	70.3
0	33.5	110	675	57	2.45	815	100	100.0
0.35	37.3	130	840	58	2.47	850	115	100.0

In the sections to follow, the still temperature has varied from ~ 0.73 K to ~ 0.85 K. This variation can be attributed to making changes to the DR to troubleshoot and evaluate performance, in addition to changing the experimental heat load on the cryostat and the still. Typically for each cool-down, evaluation of the DR was done in parallel with a separate experiment loaded on the DR.

3.8   Optimization and Improvements

3.8.1   Troubleshooting the Poor Base Temperature

The current base temperature of 70 mK is significantly higher than *Oxford's* specification value of 6.5 mK (at a ^{3}He circulation rate of 200 mumols/sec) for the *Oxford* 200 dilution unit (see Appendix A). However, a direct comparison to this value may no longer be valid due to the different arrangement and operation (wet to dry style). Operating in the dry configuration means the incoming liquid temperature to the dilution unit is much higher (~ 2.5 K instead of ~ 1 K). Since no other heat exchangers were added to the dilution unit, the incoming liquid may not be able to cool sufficiently before reaching the mixing chamber. This would cause a large return heat load on the mixing chamber, effectively increasing the base temperature. To evaluate if this return heat load was the cause of the poor base temperature, the DR was put into "one-shot" mode. In one-shot mode, a valve near the cryostat is closed in order to stop returning ^{3}He. In addition, heat is applied to the still to maintain the ^{3}He circulation rate and thus the cooling power in the mixing chamber. A one-shot requires the still to have a significant amount of liquid (^{3}He dilute phase) to give enough time to measure temperature changes in the mixing chamber. For a DR functioning properly, a minor amount of cooling (improved base temperature) of the mixing chamber occurs due to the lack of return heat load. In fact, one-shotting is commonly used as a single shot technique to reduce the base temperature of the DR even further. Several one-shots were performed with no measurable improvement of the base temperature observed. This result was unexpected, suggesting the return heat load not to be the issue.

Moving forward, other possible reasons considered for the poor base temperature were thermometry, mechanical vibrations from the PTR or GHS and internal issues with the *Oxford* 200 dilution unit. Since only secondary (resistance) thermometers were employed on the DR, incorrect reading caused by self heating of the resistance thermometers cannot be fully eliminated. Although efforts to avoid self-heating caused by noise or thermometry excitation were performed, the deviation observed in the mixing chamber cooling power curve (Fig. 3.9 (b)) is consistent with self-heating. Self-heating could be evaluated by implementing a primary thermometer, such as a nuclear orientation thermometer. Heat from mechanical vibrations caused by PTR was evaluated by momentarily turning off the PTR during a one-shot. No improvement (cooling) of the base temperature was observed as a result of this test. Mechanical vibrations from the pumping line could be reduced by isolating the rotary pump from the diffusion pump and/or by implementing a double gimbal system, like the design outlined by Kirk *et al.* [25]. Lastly, internal issues with the *Oxford* 200 dilution were considered. Two issues can arise with the dilution unit: contamination of the metal powdered sinter in the step heat exchanger/mixing chamber and/or an internal leak between the incoming/outgoing liquid streams in one of the heat exchangers. The sinter most likely has some level of contamination as the dilution unit was open to the atmosphere for several years. Since first getting the DR running, the base temperature has steadily improved from ~ 100 mK to the current temperature of 70 mK. Over the several cool down cycles, the dilution unit was pumped on at room temperature to remove frozen-out contamination not captured by the charcoal trap on the PTR 1st stage, such as hydrogen. One explanation for the improved base temperature could be a result of pumping on the dilution unit repeatedly, thereby cleaning the sinter and improving the performance. Evaluating a leak in the dilution unit is significantly more involved, but possible. Indium seals are used at each cold stage of the dilution unit. Thus, by blanking off stages and leak checking, one can determine a heat exchanger section where the leak is. Finding the leak may be possible but fixing it would be very technically challenging, requiring precision welding/soldering inside one of the heat exchangers. As an alternative to troubleshooting internal issues with the dilution unit, the unit was replaced with another wet style, decommissioned *Oxford* 200 dilution unit from the NRC group. Unfortunately, the base temperature reached was exactly the same, 70 mK. This strongly suggests the

45

previous dilution unit had no issues and the dilution unit is not the cause of the poor base temperature.

3.8.2   Evaluation of Direct PTR Pre-Cooling

The performance of the condensation stages outlined in Section 3.1 can be characterized by estimating the amount of heat load on the still caused by re-condensation of ^{3}He. If the (incoming) return line is well heat-sunk, the ^{3}He temperature exiting the last heat exchanger (before the main flow impedance) should approximately equal the PTR 2nd stage temperature (~ 2.5 K). If the return line is insufficiently heat-sunk, the return heat load on the still will be too large, preventing ^{3}He condensation to a liquid. Alternatively, if the return heat load dominates the total still cooling power, the still will be unable to hold liquid, resulting in the system being unstable.

As mentioned earlier, the return heat load can be evaluated by putting the DR into one-shot mode. By stopping the recirculation of ^{3}He, the return heat load on the still is eliminated, causing the still to cool. By applying a known amount of still heat during this process, the still temperature can be maintained at the same value before the start of the one-shot. The heater power required to achieve the same still temperature provides an estimate of the return heat load. In this work, the return heat load was found to be ~ 0.1 mW for a ^{3}He circulation rate of 120 μmols/sec. As a comparison, the cooling power of the still for this circulation rate is ~ 4 mW ($\dot{Q} = \dot{n}L$, $L_{^3\text{He}}(0.8K) \sim 33 J/mol$). In steady state, the remaining heat load (~ 3.9 mW) on the still can be attributed to radiation, the still pumping line, wiring, and coaxial cables. Evaluating if the DR could operate at higher circulation rates is not possible due to the high still temperature (~ 815 mK with no still heat). Before this could be evaluated, the still must be pumped better to operate at a lower temperature ≤ 0.7 K for the current circulation rate of 120 μmols/sec. With improved still performance, the circulation rate could be increased by applying still heat and the maximum circulation rate could be empirically determined.

The theoretical maximum circulation rate will depend on the limiting factor of either the performance of the condensation stages or the value of the main flow impedance. When the circulation rate increases, the heat load on the condensation stages and still also

46

increases. In the still, the cooling power increases by the same amount as the increase in the return heat load. However, the heat exchangers throughout the system become less effective for higher circulation rates. The increased heat load on the heat exchangers begins to challenge the thermal links between the gas and the heat exchanger and the heat exchanger to the cold stage. For this system which possesses several heat exchangers at different cold stages, all with different geometries, no simple analytical model can be used for determining the heat exchanger efficiency as a function of circulation rate. Alternatively, the main flow impedance could be too large, limiting the incoming ^{3}He flow. Distinguishing the limiting factor could be achieved by placing a thermometer at the output of the last PTR heat exchanger (i.e., before the main flow impedance) and measuring the temperature as a function of circulation rate. If the temperature increases significantly with increasing circulation rate, this may suggest that the PTR condensation stages are the limiting factor to the circulation rate. If instead the output temperature remains roughly constant, but the condensing pressure increases, this may suggest that the impedance may be the limiting factor to the circulation rate.

3.8.3   Adjusting the Mixture Amount/Ratio

The dilution unit (*Oxford* 200) was originally configured on a commercial wet style DR made by *Oxford instruments* in 1985. *Oxford* supplies the correct ^{3}He - ^{4}He mixture amount and ratio according to the total system volume. During operation, typically a small amount of ^{3}He will exist in the GHS and in the connections to the cryostat. According to the ideal gas law ($PV = nRT$), the number of moles of gas n depends on the pressure ($P \propto n$). The still pumping line operates under high vacuum (~ 0.05 mbar) and therefore has a negligible contribution. However, for the incoming (return) line to the cryostat, the pressure is much higher and is set by the required condensation pressure. For a wet style DR with a 1 K pot condenser, the condensation pressure required is very low (12 mbar for ^{3}He). However, in the dry configuration, the condensation pressure is much higher (453 mbar for ^{3}He). Thus, the difference in operation (wet to dry style) will require an extra $\sim 0.441 \cdot \mathrm{V_{sys}}$ Litres of ^{3}He at standard temperature and pressure (STP). In addition, the physical volume of the condensation stages is also different. While difficult to accurately measure the volume

difference, it is estimated that the volume has increased predominantly due to the charcoal trap located on the PTR 1st stage. Therefore, it was important to re-calibrate the mixture amount/ratio to ensure the phase boundary was in the mixing chamber. If the phase boundary is in the step heat exchanger, the base temperature and cooling power will be significantly reduced.

A series of steps were taken to accurately determine the correct amount/ratio of the mixture in this new dry configuration. The text of Richardson and Smith provides an excellent detailed troubleshooting guide to adjust the amount/ratio of the mixture. [24]. An indication of the mixture amount comes from the still temperature and nominal ^{3}He circulation rate $\dot{n}$. If too much mixture is in the system, the liquid level in the still will be up in the still pumping line. This will cause the still to run hot with little cooling power but have a high circulation rate. If instead too little mixture is in the system, the liquid level will be down inside the continuous counterflow heat exchanger. This will also cause the still to run hot (≥ 1 K) with a very low circulation rate (≤ 60 μmols/sec) due to the reduced surface area.

On the first successful cool-down using the stock mixture, the still temperature was high (~ 1.3 K) and the circulation rate was low ($\dot{n} \sim 80$ μmoles/sec). This was consistent with the still being empty (i.e., no liquid), which was expected. ^{3}He was then added from a compressed gas cylinder to effectively push the phase boundary towards the still. This should also push the ^{3}He dilute side liquid level into the still, enabling the still to hold liquid. A drop in still temperature (~ 1.3 K to ~ 0.75 K) and increased circulation rate (~ 80 μmoles/sec to ~ 120 μmoles/sec) was observed after adding ^{3}He. Slightly more ^{3}He was added to partially fill the still with liquid. At this point the temperature of the mixing chamber was ~ 100 mK. Next, the DR was put into one-shot mode, as described in Section 3.7.2. In this case, a one-shot was performed to detect the location of the phase boundary. As a consequence of one-shotting, the phase boundary will move towards the return side (^{3}He concentrated side) as the amount of condensed ^{3}He in the dilution unit is slowly removed. An abrupt and sudden cooling of the mixing chamber should occur if the phase boundary location moves from the step heat exchanger into the mixing chamber (on the ^{3}He dilute side). Unfortunately, no cooling of the mixing chamber occurred. This was very unexpected, as some cooling should occur just from the lack of return load. Moving

forward, additional ³He was added until, by rough calculation, the mixture ratio was close to 50% ³He by volume. The idea was to push the system into a state of excess ³He, ensuring the phase boundary was on the output of the mixing chamber (³He dilute side). With too much ³He, several one-shots were performed. However, instead of re-condensing the ³He pulled out, it was stored in a separate container and ⁴He was added to replace it (refilling the still with liquid). Replacing ³He with ⁴He will cause the phase boundary to move towards the return (³He concentrated) side of the dilution unit. After several one-shots, the mixing chamber began to warm, indicating the phase boundary had now moved into the step heat exchanger on the return side.

With no improvement in base temperature throughout this process, it became clear that the phase boundary was in the mixing chamber all along. The poor base temperature must instead be caused by self heating of the resistance thermometers, vibrations from the GHS or an internal issue with the *Oxford* 200 dilution unit. Nevertheless, the mixture amount and ratio was optimized for a fast cool-down. This consisted of using the least amount of mixture possible (minimum liquid level in the still) and also the least amount of ³He (which is difficult and time consuming to condense).

3.8.4   Still Pumping Line Conductance

A key performance metric of a DR is the volumetric throughput of the pumping system. As described in section 2.3.3, the cooling power of the still is proportional to the vapour pressure above the liquid surface. Thus, for a low still temperature at a high circulation rate, a high pumping throughput is needed. A key design consideration that is often overlooked is the still pumping line connecting the top of the cryostat to the series of pumps. A common design flaw is employing a high throughput series of pumps but "choking" the pumps by connecting an insufficient pumping line to the cryostat. In addition to providing a conduit for gas flow, the pumping line should also include a mechanism for vibration and electrical isolation. Electrical noise from the GHS/pumps should be isolated to prevent disturbance of the ground of the cryostat. Electrical isolation is achieved by employing a section of PVC pipe and/or a plastic centering ring for the KF rubber O-ring flange joining two pipes. Vibrations from the rotary pump should also be isolated from the

cryostat and can be achieved by implementing a double gimbal system. The use of an oil vapour diffusion pump (like in this work), which has no moving parts (i.e., no vibrations), can also reduce vibrations from being produced on the pumping line. A brief overview of the key properties of pumping systems will be described. Further details can be found in the texts of O'Hanlon [3] and Richardson and Smith [24].

To characterize the efficiency of a vacuum system, it is first necessary to determine the flow regime which the system will operate under. The flow regime depends on the properties of the gas itself in addition to the relative quantity of the gas flowing. For high vacuum (i.e., low pressure), the mean free path is much greater than the pipe diameter and the flow is molecular. For low vacuum (i.e., high pressure), the mean free path is much less than the diameter of the pipe and the flow is viscous. A dimensionless quantity known as the Knudsen number is used to quantitatively describe these two regimes

$$Kn = \frac{\lambda}{L} \tag{3.6}$$

where λ is the mean free path and L is a characteristic length scale of the system. In the context of long round pipes, this length scale corresponds to the diameter of the pipe. The mean free path of a molecule in a gas is given by

$$L = \frac{k_B T}{\sqrt{2}\pi d^2 P} \tag{3.7}$$

where T and P are the temperature and pressure of the gas, d is the equivalent hard-sphere diameter of the molecule and k_B is the Boltzman constant. Viscous flow occurs for $Kn < 0.01$ and molecular flow occurs for $Kn > 1$. A transition regime occurs between these two extremes and is known as Knudsen flow. An illustration of the different flow regimes is shown in Fig. 3.10.

For viscous flow, resistance occurs due to interactions between gas molecules themselves in addition to interactions with the walls of the pipe. In molecular flow, the resistance is dominated by interactions with the walls of the pipe. Instead of flow resistance for pumping connections, it is customary to discuss the reciprocal or flow conductance, which has units
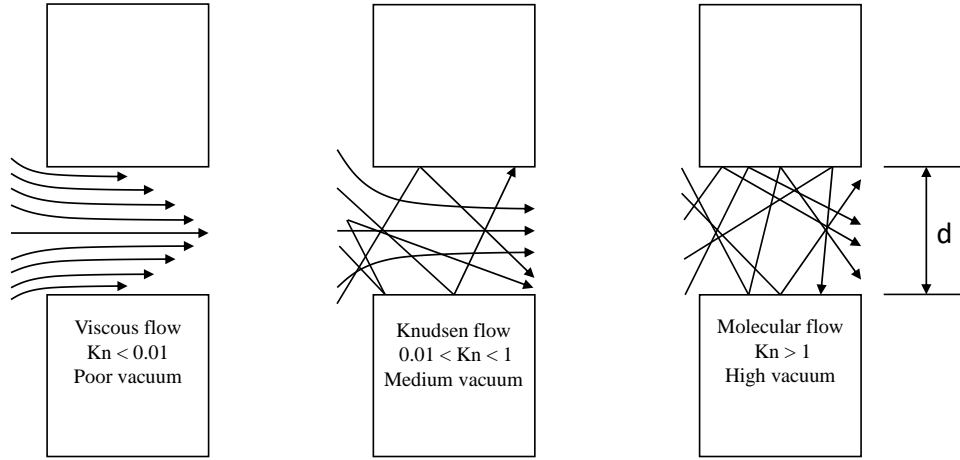
Figure 3.10: Profiles of the various flow regimes for a pipe of diameter d. Adopted from [4].

of volume per unit time (e.g., L/sec). For viscous flow, the conductance depends linearly with the average pressure P_{avg} in the pipe

$$C_{vis} = \frac{\pi r^4}{8\eta\ell} P_{avg} \tag{3.8}$$

Where r is the radius of the pipe, η is the viscosity of the gas and ℓ is the length of the pipe. For molecular flow, the conductance has no pressure dependence and is given by

$$C_{mol} = \frac{4r^3}{3l}\sqrt{\frac{2\pi k_B T}{m}} \tag{3.9}$$

Where k_B is the Boltzman constant and T, m is the temperature and mass of the gas, respectively. For Knudsen flow, the conductance is a combination of viscous and molecular flow

$$C_{Kn} = C_{vis} + \beta C_{mol} \tag{3.10}$$

Where β is a coefficient that is no greater than unity and depends on the gas temperature, pressure, viscosity and the pipe diameter. When multiple pipes are joined together in series, the total conductance is given by

$$\frac{1}{C_{tot}} = \frac{1}{C_1} + \frac{1}{C_2}... + \frac{1}{C_n} \tag{3.11}$$

For the still pumping line on a DR, typically Knudsen (intermediate) flow exists. However, when designing a pumping line, one should design it assuming molecular flow. From Eq 3.10, following this rule will result in the actual throughput being greater than or equal to what is calculated assuming molecular flow.

In addition to the flow conductance, two other useful quantities are the pumping speed S and the throughput Q. A vacuum pump is defined by its pumping speed, measured for a certain (limited) inlet pressure to the pump. Pumping speed also has units of volume per unit time (e.g., L/sec), but is different from conductance in that it is an empirically determined performance characteristic of a vacuum pump. Throughput is defined as the volume of gas crossing a plane per unit time, multiplied by the pressure at the plane. It has units of pressure-volume per unit time (e.g., mbar·L/sec). The throughput of a vacuum pump can be written as the product of the inlet pressure and the pumping speed, increasing linearly with pressure up to some maximum inlet pressure.

In this work, the diffusion and rotary pumps are housed inside the GHS which are located $\sim$ 6 m away from the cryostat. Since the GHS was designed to be portable, the unit came with a flexible KF-50 ($\sim$ 3.7 m long, 5 cm ID) bellows to connect to the cryostat. This bellows was initially used, with additional short $\sim$ 1 m lengths of KF-50 bellows on either side to connect to the cryostat and GHS. Using Eq 3.9, the molecular flow conductance for ^{3}He gas at 300 K with this configuration was $\sim$ 8 L/sec. As a comparison, the stock Edwards diffusion pump has a pumping speed of 850 L/sec, according to the specification sheet. Clearly, the diffusion pump is severely choked with this pumping line. In an effort to improve the room temperature pumping line, the long ($\sim$ 3.7 m) KF-50 bellows was replaced with a rigid, 3" (7.6 cm) ID PVC pipe. With this new arrangement, the molecular flow conductance of the room temperature pumping line is $\sim$ 14 L/sec.

With less than a factor of 2 improvement in overall conductance of the room temperature segment, no significant increase in performance was measured.

For the current pumping line described, the still temperature is $\sim$ 0.85 K for a ^{3}He circulation rate of 120 μmoles/sec. To estimate the dimensions of a larger pumping line that will give improved still performance, it is necessary to calculate which pumping line segment (room temperature or inside the cryostat) is the dominant source of flow resistance. For the segment of pumping line inside the cryostat, the average pressure (temperature) of the gas is higher (lower) when compared to the segment of pumping line in the room. Under these conditions, calculation of the Knudsen number gives Kn $\sim$ 1 x 10^{-5}, or viscous flow. Thus, using the dimensions of the pumping line segment inside the cryostat (7/8" ID, 30 cm long + 5 cm ID, 12 cm long) gives a viscous flow conductance of $\sim$ 9 L/sec. However, since the temperature of the gas exiting the still and in the pipe is low $\sim$ 3 K, the density (mol/L) of the gas is $\sim$ 100 times larger than the gas would be at room temperature (300 K). Thus, the effective conductance of this pumping line is $\sim$ 100 larger or $\sim$ 900 L/sec. The calculated high conductance for the dimensions of this pipe segment is consistent with other still pipes inside the cryostat used in commercial DRs. This calculation clearly suggests the room temperature pumping line to be the dominant flow resistance. Using the current performance of the still, an estimate can be made to determine the required size (diameter) of pumping line in the room necessary to have a still temperature of 0.65 K. Based off of the current still temperature, the corresponding ^{3}He vapour pressure in the still is $\sim$ 5.3 mbar. Since the pumping speed of the diffusion pump is very large (850 L/sec), the pump can be assumed to generate a near perfect vacuum (i.e., zero pressure) at its inlet. From this assumption, the conductance of the entire pumping line can be estimated. The gas flow through a pipe can be treated analogously to electrical current flowing through a conductor. Ohm's law is given by

$$G = \frac{I}{V} \tag{3.12}$$

Where G is the electrical conductance, I is the current and V is the voltage drop. Similarly, for gas flow in a pipe, the conductance is proportional to the molar flow rate $\dot{n}$ and the

pressure drop ΔP in the pipe

$$C \propto \frac{\dot{n}}{\Delta P} \tag{3.13}$$

Applying the ideal gas law gives

$$C = \frac{\dot{n}}{\Delta P} RT \tag{3.14}$$

Where R is the ideal gas constant and T is the temperature of the gas. For a still temperature of 0.65 K, the ^{3}He vapour pressure in the still must be ~ 1.2 mbar, or a factor of ~ 4.4 lower than what it is currently (5.3 mbar). To achieve this pressure drop ΔP while maintaining the same circulation rate $\dot{n}$, the total conductance C of the system must increase by a factor of 4.4 (Eq 3.14). Applying Eq 3.11, the total conductance of the current system is given by

$$C_{sys} = \frac{1}{1/S_{pump} + 1/C_{RT} + 1/C_{cold}} = \frac{1}{1/850 + 1/14 + 1/900} = 14.2 \; L/sec \tag{3.15}$$

A factor of 4.4 improvement corresponds to a total system conductance of ~ 62 L/sec. To achieve this, the conductance of the room temperature pumping line (C_{RT}) must increase to ~ 72 L/sec. Keeping the pumping line the same length as it is currently, one approach would be to implement a larger diameter and longer PVC pipe while shortening the KF-50 connections to the cryostat and GHS. To achieve a conductance of 72 L/sec, the current PVC pumping line (3" ID, 3.7 m) could be changed to a 6" ID, 5.4 m long PVC pipe and the KF-50 connections to cryostat and GHS can be shortened to just 23 cm. Alternatively, a maximum (within practical reason) total conductance of ~ 120 L/sec could be achieved by replacing the current PVC pipe pumping line to a 8" ID, 5.7 m long PVC pipe and the KF-50 connections to cryostat and GHS can be shortened to just 10 cm. With this level of improvement, the still temperature for the current circulation rate would be 0.59 K.

3.9 Conclusions

In summary, the Shasta cryostat was successfully adapted from an ADR to a dry style DR. In contrast to the wet style DR, the dry style DR is a cost effective and self sufficient system. While optimal performance was not achieved with respect to the base temperature, this system still outperforms the previous ADR for temperatures above 70 mK. The DR is capable of continuously regulating a temperature of 100 mK with 33 μW of applied heat. In contrast, regulating the ADR (FAA salt) at a temperature of 100 mK, the cooling capacity is limited to $\sim$ 100 mJ. As a comparison, the ADR at 100 mK could sustain 33 μW of applied heat for $\lesssim$ 50 minutes before beginning to warm up.

The cause of the poor base temperature has been investigated. From the performance data, the poor base temperature is consistent with a continuous heat load of $\sim$ 23 μW on the mixing chamber. As a result of this work, the following has been eliminated as potential causes: ^{3}He return heat load, the phase boundary not being in the mixing chamber and internal issues with the *Oxford* 200 dilution unit. Other options that have been investigated, but not ruled out, are self-heating of the resistance thermometers and heating caused by vibrations from the PTR and/or GHS.

3.10 Future Work

Moving forward, the conductance of the pumping line could be improved to reduce the vapour pressure in the still, resulting in a lower still temperature ($<$ 0.7 K) for the current circulation rate of $\sim$ 120 μmols/sec. By applying still heat, the circulation rate could be increased and the limiting factor (condensation stages or the main flow impedance) for the circulation rate could be determined. A primary thermometer, such as a nuclear orientation thermometer, could be implemented to evaluate if the poor base temperature is a result of self-heating of the resistance thermometers currently employed. Heating caused by vibrations from the GHS could be reduced by mechanically isolating the rotary pump from the diffusion pump and/or by implementing a double gimbal system.

Part II

Measurements on Superconducting Devices

Chapter 4

Superconducting Microwave Resonators

4.1 Introduction

The discovery of superconductivity in 1911 by Heike Kammerlingh Onnes was a historic moment in physics. A theoretical framework to explain the phenomena proved difficult, taking nearly 50 years to explain the microscopic effect. The now famous framework known as BSC theory, developed by Bardeen, Cooper, and Schrieffer [26] in 1957, accurately describes the behaviour of conventional superconductors which are typically elemental metals. Qualitatively, the theory describes how electrons group together to form pairs, mediated by a phonon interaction with the lattice of the material. These electron pairs are known as Cooper pairs and have a net integer spin, a property which allows them to Bose condense into the quantum mechanical ground state at low temperatures. Each material has its own critical temperature (T_c) and critical field (H_c), above which the superconducting state is destroyed. Due to the small energy scales required to form the superconducting state, the effect is limited to low temperatures (< 10 K) for conventional superconductors. Conventional superconductors are used in the low temperature physics laboratory with the fabrication of superconducting devices.

Superconducting resonators are a class of superconducting devices that have gained significant interest in the last two decades in the fields of quantum computing and radio astronomy. Improved materials and fabrication processes have enabled these devices to achieve very low losses. Characterization measurements on these devices are a valuable tool in working towards reducing losses to the theoretical minimum. The work presented here details the first steps to characterizing performance of these resonators. The ultimate goal was to setup a measurement system to study the loss mechanisms in these resonators. This will lead to a better understanding of the underlying physics in addition to improving them for use in quantum circuits.

4.2   Relevance for Quantum Computing

The Josephson junction is a superconducting circuit element that has become an integral part of quantum computing devices and qubit architectures. The geometry is analogous to that of a parallel plate capacitor, comprised of two superconductors separated by a thin insulating layer, normal metal or by a narrow constriction [27]. It is used in quantum devices, such as the superconducting quantum interference device (SQUID) and is also the primary circuit element in the charge, phase and flux superconducting qubit architectures. In these applications, the type of tunnel barrier typically implemented is a thin insulating layer, such as aluminum oxide. The structural arrangement of the oxide layer is amorphous in nature. Such amorphous materials behave much differently than periodically ordered crystals at low temperatures. At low temperatures, the disordered structure of amorphous materials enables atoms and/or groups of atoms to effectively tunnel between different locations within the material. This extra degree of freedom is reflected in measurements of specific heat, where an additional roughly linear T dependence dominates over the Debye T^3 phonon contribution at low temperatures [2]. In superconducting qubits, these transitions can couple to the qubit, resulting in loss channels which ultimately lead to decoherence.

4.3 Types of Resonators

Superconducting resonators are fabricated on the micron scale using modern lithography techniques. One of the simplest and most common type of superconducting resonators consists of a transmission line in a co-planar waveguide (CPW) geometry, as shown in Fig. 4.1 (a).

(a) Coplanar waveguide (CPW) geometry

(b) Quarter-wavelength ($\lambda/4$) resonator
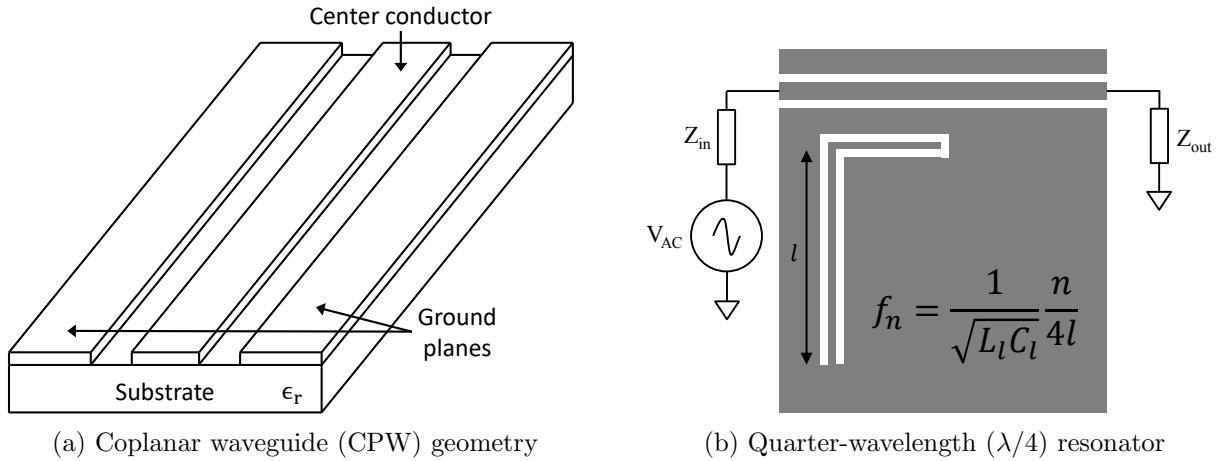
Figure 4.1: (a) Standard coplanar waveguide (CPW) geometry. (b) Quarter-wavelength ($\lambda/4$) resonator, transmission line coupled to coplanar feedline.

The CPW consists of a metallic thin film separated into a center conductor and ground planes on either side. This metallic film sits on top of a dielectric substrate. A resonator in a CPW geometry is characterized by a distributed element circuit model. In this model, the values of inductance, capacitance and resistance are spread throughout the circuit rather than at discrete locations within it. In general, it is possible for transmission lines to support modes without transverse electromagnetic (TEM) field components. A superconducting CPW cannot support a pure TEM mode, but can support a quasi-TEM wave with velocity given by [28]

$$v = \frac{c}{\sqrt{\epsilon_{eff}}} = \frac{1}{\sqrt{L_l C_l}} \tag{4.1}$$

where c is the speed of light, ϵ_{eff} is the effective permittivity and L_l and C_l are the inductance and capacitance per unit length, respectively. Two common CPW resonators are the half-wavelength ($\lambda/2$) and quarter-wavelength ($\lambda/4$) resonator. Such resonate structures can support a set of sinusoidal standing waves, where the locations of the nodes and anti-nodes are determined by the terminating component. The $\lambda/2$ resonator is typically terminated and capacitively coupled to the transmission line. In this case, the fundamental resonance frequency is $f_1^{1/2} = \upsilon(2\ell)^{-1}$. The $\lambda/4$ resonator is typically open on the end that is coupled to the transmission line and grounded at the other end (Fig. 4.1 (b)). In this case, the fundamental frequency is given by $f_1^{1/4} = \upsilon(4\ell)^{-1}$. In both the $\lambda/2$ and $\lambda/4$ resonators, m linear harmonic modes $f_m = mf_1$ exist for odd value of m.

The simplicity of the CPW geometry enables ease of fabrication: requiring deposition of only a single metal layer onto a high quality crystalline substrate. The importance of the substrate and/or avoidance of additional insulating layers will be discussed in later sections. In addition, several quarter-wavelength resonators operating at different resonant frequencies can be measured simultaneously (frequency multiplexed) when coupled to a shared feedline. This frequency multiplexing technique is employed in large resonator arrays for astronomical radiation detectors, known as microwave kinetic inductance detectors (MKID) [29].

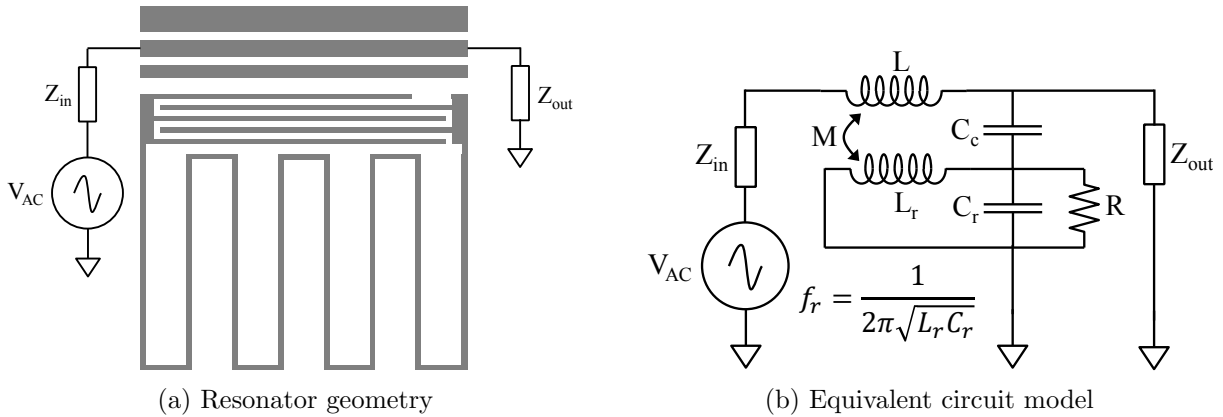(a) Resonator geometry   (b) Equivalent circuit model

Figure 4.2: Lumped element resonator geometry (a) and circuit model (b). Adopted from [5].

A second type of resonator geometry is known as the lumped element structure. Contrary to the CPW resonator, the circuit elements are individually "lumped" together in a more traditional circuit layout. Figure. 4.2 (a) is an example of such a structure, which consists of an etched interdigitated capacitor and meandered line inductor geometry. The equivalent circuit is depicted in Fig. 4.2(b). The resonator is coupled to a transmission line with inductance L through a coupling capacitance C_c and mutual inductance $M = k\sqrt{LL_r}$, where k is a geometric factor. Just like the $\lambda/4$ CPW resonator, this resonator layout also supports frequency multiplexing.

4.4   History of Excess Noise

The total quality factor Q_r is a measure of the loss of a resonant circuit and is defined by

$$Q_r = 2\pi \frac{\text{average stored energy}}{\text{energy loss in one period}} \tag{4.2}$$

A high Q_r value corresponds to low losses in the resonant circuit. In microwave resonators, losses arise from dissipative mechanisms (Q_i) in addition to coupling to the main feedline (Q_c)

$$\frac{1}{Q_r} = \frac{1}{Q_c} + \frac{1}{Q_i} \tag{4.3}$$

While very high-quality factors $Q_r \sim 10^6$ have been demonstrated for 2D planar geometries [30], further work is required to resolve the residual dissipation in these devices. An intrinsic non-zero dissipative mechanism occurs for superconductors subjected to an external AC field. This effect was first proposed by Heinz London [31] and considers the finite inertia of Cooper pairs that gives rise to AC electric fields inside the superconductor. For finite temperatures, the fraction of normal electrons in the superconductor can couple to this AC field and thus dissipate energy. BSC theory [32, 26] enabled a quantitative description of London's proposal, which was published soon after [33, 34] and is known as the Mattis-Bardeen theory. This theory enables the calculation of the complex

conductivity and the corresponding surface impedance of a superconducting film. Their theoretical description shows that dissipation can be reduced by operating at sufficiently low temperatures, where the relative density of quasiparticles is small compared to Cooper pairs. Thus, this theory provides a lower limit to the dissipation in these devices.

Performance of superconducting resonators has improved steadily over the last few decades due to better materials, fabrication methods and experimental conditions [35]. However, in the early 2000s, measurements on superconducting resonators at Caltech and the Jet Propulsion Laboratory (JPL) showed significant deviation from the Mattis-Bardeen theory [36]. In 2005 it was proposed (and later demonstrated) that the excess noise observed may be generated by two-level tunneling systems in the amorphous dielectric materials used as the substrate [7]. Two-level systems (TLS) are tunneling states in amorphous solids and have a broad distribution of energy splitting. Fortunately, TLS have been studied since the 1960s, with a well established model developed since the 1970s [37, 38, 39]. The original TLS theory considered tunnelling of atoms or groups of atoms between two nearby equilibrium positions in amorphous materials. Silicon dioxide SiO_2 is an example of such a dielectric material that can exist in a crystalline and amorphous structure, as shown in Fig. 4.3. In the case of the dielectric substrate of superconducting resonators, the TLS are thermally activated at low temperatures and thus produce excess noise. As mentioned previously, TLS in the tunnel barrier of Josephson junctions have been found to contribute excess noise and cause decoherence in superconducting qubits [40].

Historically, planar superconducting resonators and/or the capacitive element in them were fabricated in multiple layers (i.e., superconductor, insulator, superconductor). Deposition of an insulating dielectric material results in amorphous layers capable of hosting TLS. To simplify the problem, the Caltech/JPL group made CPW resonators that consisted of a single superconducting niobium layer on a high-quality crystalline substrate, such as silicon or sapphire [7]. Since the critical temperature of niobium is $T_c = 9.2$ K and measurements are performed at temperatures < 1 K, conductivity effects from the superconductor can be neglected. This showed significant improvement in the excess noise over previous devices made with amorphous substrates/dilectric components. However, a TLS-hosting layer was, and still is, observed to be at the surface of the resonator. By varying the geometry of the CPW resonator, it was determined that the TLS layer must exist either
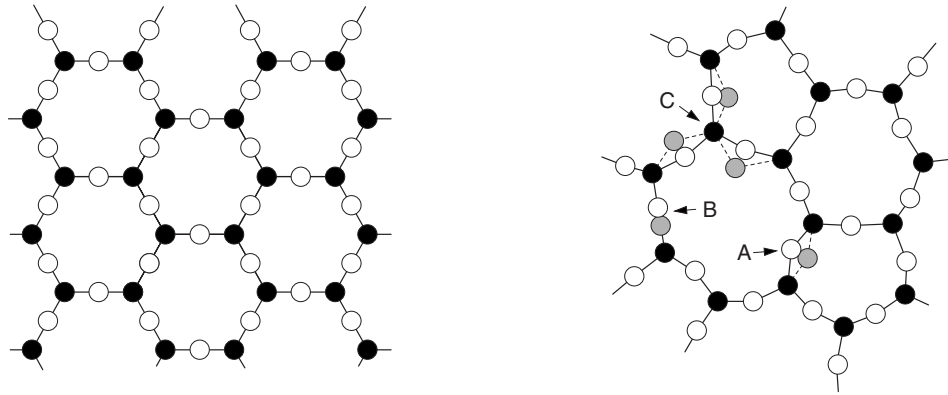
Figure 4.3: 2D structure of cyrstalline quartz (left) and amorphous vitreous silica (right) [6]. Black (white) circles represent Si (O). In the amorphous version, oxygen atoms can tunnel between two nearby equilibrium positions.

on the exposed surface of the substrate and/or as a few nanometer native oxide layer on the surface of the superconducting film[41]. Current efforts in alleviating TLS fluctuators include optimizing resonator geometry [42], using non-oxidizing superconducting silicides [43] and developing/incorporating single crystal dielectric materials [44]. Since these efforts challenge current materials and fabrication techniques, progress has been marginal, with quality factors of $Q_r \sim 10^6$ still being the maximum achieved to date. Improvement of resonator design and fabrication methods will demand high throughput, low temperature characterization. Systematic studies of these parameters will ultimately lead to improved resonators.

Chapter 5

Two-level System (TLS) Model

5.1 TLS Hamiltonian

The TLS-induced loss found in superconducting resonators can be derived from the standard TLS theory. The analysis in this chapter follows closely from the original works of Phillips [39, 38] and Anderson [37] and the secondary sources of Gao [7] and Otto [45].

A TLS can be treated quantum mechanically as a particle with mass m in a double-well potential. To simplify the problem, the double-well potential can be modelled as the overlap of two single-wells with an asymmetric energy difference Δ, as illistrated in Fig. 5.1. The energy levels of the double-well can be computed using the solutions of the single-well problem with potentials V_1 and V_2. In the localized representation, the basis states $|\phi_1\rangle$ and $|\phi_2\rangle$ are the ground states of the Hamiltonians H_1 and H_2, respectively. The double-well Hamiltonian with potential V can be written as [6, 39]

$$H = H_1 + (V - V_1) + H_2 + (V - V_2) \tag{5.1}$$

Using the Schrödinger equation $H|\psi\rangle = E|\psi\rangle$ and the ansatz $|\psi\rangle = a_1|\phi_1\rangle + a_2|\phi_2\rangle$, the
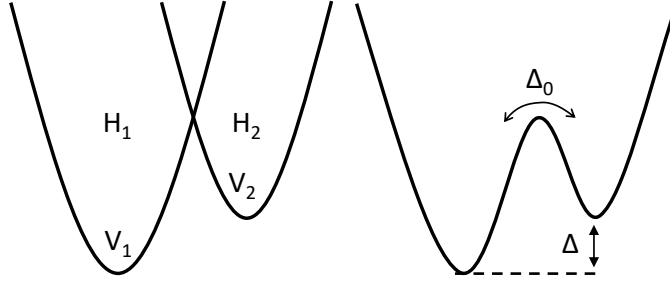
Figure 5.1: Two-level systems described by double well potentials.

eigenenergies of the double well are given by

$$E = \frac{\int \psi^* H \psi d^3 x}{\int \psi^* \psi d^3 x} = \frac{a_1^2 \langle \phi_1 | H | \phi_1 \rangle + a_2^2 \langle \phi_2 | H | \phi_2 \rangle + 2 a_1 a_2 \langle \phi_1 | H | \phi_2 \rangle}{a_1^2 + a_2^2 + 2 a_1 a_2 \langle \phi_1 | \phi_2 \rangle} \tag{5.2}$$

Where $\langle \phi_1 | H | \phi_1 \rangle \equiv E_1$ and $\langle \phi_2 | H | \phi_2 \rangle \equiv E_2$ are the energies associated with the left and right wells, respectively. The overlap of the two wells gives rise to an off-diagonal exchange energy $\langle \phi_1 | H | \phi_2 \rangle \equiv \langle \phi_2 | H | \phi_1 \rangle$. Explicitly, the matrix elements are given by

$$H_{11} = \langle \phi_1 | H | \phi_1 \rangle = \langle \phi_1 | H_1 | \phi_1 \rangle + \langle \phi_1 | V - V_1 | \phi_1 \rangle \tag{5.3}$$

$$H_{22} = \langle \phi_2 | H | \phi_2 \rangle = \langle \phi_2 | H_2 | \phi_2 \rangle + \langle \phi_2 | V - V_2 | \phi_2 \rangle \tag{5.4}$$

$$H_{12} = H_{21} = \langle \phi_1 | H | \phi_2 \rangle \tag{5.5}$$

If the overlap of the individual ground states into the barrier is small, $\langle \phi_i | V - V_i | \phi_i \rangle$ can be neglected in comparison to E_i. For single-wells that are far apart, the overlap of the wavefunctions $\langle \phi_1 | \phi_2 \rangle$ tends to zero. The energies can be determined by minimizing equation (5.2) with respect to the coefficients a_1 and a_2

$$\frac{\partial E}{\partial a_1} = 0 \rightarrow a_1 (H_{11} - E) + a_2 (H_{12} - E \langle \phi_1 | \phi_2 \rangle) = 0 \tag{5.6}$$

$$\frac{\partial E}{\partial a_2} = 0 \rightarrow a_2(H_{22} - E) + a_1(H_{12} - E \langle \phi_1 | \phi_2 \rangle) = 0 \tag{5.7}$$

Eliminating the coefficients a_1 and a_2 gives the following

$$(H_{11} - E)(H_{22} - E) - (H_{12} - (E \langle \phi_1 | \phi_2 \rangle))^2 = 0 \tag{5.8}$$

Letting the energy minima be the average of the two individual single-wells $\hbar\Omega \equiv \frac{1}{2}(E_1 + E_2)$, the eigenenergies of the two single-wells can be written as

$$E_1 = \frac{1}{2}(\hbar\Omega + \Delta) \tag{5.9}$$

$$E_2 = \frac{1}{2}(\hbar\Omega - \Delta) \tag{5.10}$$

where $\Delta = |V_1 - V_2|$. Assuming the overlap of the wavefunctions $\langle \phi_1 | \phi_2 \rangle$ is small, this term can be omitted in Eq 5.8. Combining Eq 5.8, 5.9, 5.10 the eigenenergies for the double-well are given by

$$E_{\pm} = \frac{1}{2}\left(\hbar\Omega \pm \sqrt{\Delta^2 + 4H_{12}^2}\right) \tag{5.11}$$

Thus, the energy splitting of the ground state is given by

$$E = E_+ - E_- = \sqrt{\Delta^2 + \Delta_0^2} \tag{5.12}$$

where $\Delta_0 = -2H_{12}$ is known as the tunnel splitting. Using the WKB method, Δ_0 can be evaluated for specific potentials V. Unlike crystalline materials, amorphous materials do not have a particular microscopic form for the potential. Thus, a simplified expression commonly employed is

$$\Delta_0 \approx \hbar\Omega e^{-\lambda} \tag{5.13}$$

$$\lambda = -d(2mV_0/\hbar^2)^{1/2} \qquad (5.14)$$

where λ is known as the tunnelling parameter, m is the mass of the particle in the tunnelling system, d is the separation between the wells and V_0 is the barrier height. In the local basis formed by ϕ_1 and ϕ_2, the Hamiltonian can be written as

$$H = \frac{1}{2} \begin{pmatrix} -\Delta & \Delta_0 \\ \Delta_0 & \Delta \end{pmatrix} \qquad (5.15)$$

Diagonalizing the Hamiltonian in the basis formed by $|\phi_1\rangle$ and $|\phi_2\rangle$ yields

$$H = \frac{1}{2} \begin{pmatrix} -E & 0 \\ 0 & E \end{pmatrix} = -\frac{1}{2}E\sigma_z \qquad (5.16)$$

where the energy E is given by equation (5.12) and the Pauli matrices are given by

$$\sigma_x = \begin{pmatrix} 0 & 1 \\ 1 & 0 \end{pmatrix}, \quad \sigma_y = \begin{pmatrix} 0 & -i \\ i & 0 \end{pmatrix}, \sigma_z = \begin{pmatrix} 1 & 0 \\ 0 & -1 \end{pmatrix} \qquad (5.17)$$

In this basis, the normalized eigenstates for the double-well TLS potential are given by

$$|\psi_1\rangle = \cos(\theta)|\phi_1\rangle + \sin(\theta)|\phi_2\rangle \qquad (5.18)$$

$$|\psi_2\rangle = \sin(\theta)|\phi_1\rangle - \cos(\theta)|\phi_2\rangle \qquad (5.19)$$

where the energies of $|\psi_1\rangle$ and $|\psi_2\rangle$ are E and $-E$, respectively and $\tan(2\theta) = \Delta_0/\Delta$.

5.2 TLS Dynamics

TLS can interact via an external electric field $\vec{E}$ in addition to an external strain field e. As an approximation, the local electric and strain fields can be taken to be uniform [39].

For these uniform fields, the dominant effect of the external field interacting with the TLS is through the asymmetry energy Δ between the two wells, while changes in the height of the barrier Δ_0 can be neglected. In the diagonal basis formed by $|\psi_1\rangle$ and $|\psi_2\rangle$, the total (electric and strain) interaction Hamiltonian can be written as

$$H_{int}^{tot} = H_{int}^{\vec{E}} + H_{int}^{e} \tag{5.20}$$

$$H_{int} = \left| \frac{\Delta}{E}\sigma_z + \frac{\Delta_0}{E}\sigma_x \right| (\vec{p}_0 \cdot \vec{E} + \gamma e) \tag{5.21}$$

where p_0 and γ are the dipole couplings of the TLS with the electric and elastic strain field, respectively. p_0 characterizes the ability of the TLS to couple to external photons under an applied electric field $\vec{E}$. Similarly, γ characterizes the phonon coupling of the TLS, which enables relaxation processes to occur. The dynamics can be understood by noticing the analogous problem of a spin 1/2 system in a magnetic field, the Hamiltonian of which can be written as [7]

$$H = -\hbar\gamma(\vec{B}_0 \cdot \vec{S} + \vec{B}'(t) \cdot \vec{S}) \tag{5.22}$$

where $\vec{B}_0$ and $\vec{B}'(t)$ are the static and oscillating (perturbation) field and the spin operator is given by $\vec{S} = \vec{\sigma}/2$. Explicitly, the correspondence to the TLS problem is

$$-\hbar\gamma\vec{B}_0 = (0, 0, \epsilon) \tag{5.23}$$

$$-\hbar\gamma\vec{B}'(t) = (p_x, 0, p_z) \cdot \vec{E} \tag{5.24}$$

where $\vec{p}_x = 2\vec{p}_0\frac{\Delta_0}{\epsilon}$ is the transition electric dipole moment and $\vec{p}_z = \vec{p}_0\frac{\Delta}{\epsilon}$ is the permanent electric dipole moment. Ignoring relaxation processes, the time evolution for a free spin in a magnetic field is given by

$$\frac{d}{dt}\vec{S}(t) = \gamma\vec{S} \times \vec{B} \tag{5.25}$$

When longitudinal (T_1) and transverse (T_2) relaxation processes are considered, the evolution of the spin ensemble behaves according to following differential equations

$$\frac{d}{dt}\langle S_x(t)\rangle = \gamma(\langle S_y\rangle B_z - \langle S_z\rangle B_y) - \frac{\langle S_x\rangle}{T_2} \tag{5.26}$$

$$\frac{d}{dt}\langle S_y(t)\rangle = \gamma(\langle S_z\rangle B_x - \langle S_x\rangle B_z) - \frac{\langle S_y\rangle}{T_2} \tag{5.27}$$

$$\frac{d}{dt}\langle S_z(t)\rangle = \gamma(\langle S_x\rangle B_y - \langle S_y\rangle B_x) - \frac{\langle S_z\rangle - \langle S_z^{eq}\rangle}{T_1} \tag{5.28}$$

where Eq's. 5.26, 5.27, 5.28 are the famous Bloch equations originally derived to describe nuclear magnetic resonance [46]. In steady state, the instantaneous equilibrium value of S_z is given by

$$S_z^{eq} = \frac{1}{2}\tanh\left(\frac{\hbar\gamma B_z(t)}{2k_B T}\right) \tag{5.29}$$

The Bloch equations can be solved by setting up the direction of static and time dependent magnetic fields

$$\vec{B}_z = B_0 + 2B'\cos(\omega t), \ \ \vec{B}_x = 2B'\cos(\omega t) \tag{5.30}$$

The solutions can be analytically solved for small deviations to thermal equilibrium. This is achieved by linearizing Eq. 5.29 by Taylor series expansion. Since the perturbation field in Eq. 5.30 is time harmonic, the solution can be written using a Fourier series expansion over the frequency components

$$\langle S(t)\rangle = \sum_{m=-\infty}^{\infty} S_m e^{i\omega_m t} \tag{5.31}$$

where $\omega_m = m\omega$. Using Eq's 5.31,5.30, the Bloch Eq for $\langle S_z(t)\rangle$ yields a set of coupled linear equations for S_m. It has been shown that only the $m = $ -1, 0, +1 are important near

resonance. As a result, the Fourier components needed to describe the system are given by [47]

$$S_x(\omega) = -\frac{S_z^0}{2\hbar} \left(\frac{1}{\omega_0 - \omega + iT_2^{-1}} + \frac{1}{\omega_0 + \omega - iT_2^{-1}} \right) \hbar\gamma B_x \qquad (5.32)$$

$$S_z = \frac{dS_z^0}{d(\hbar\eta B_0)} \frac{1 - i\omega T_1}{1 + \omega^2 T_1^2} \hbar\gamma B_z \qquad (5.33)$$

and

$$S_z^0 = \frac{1 + (\omega_0 - \omega)^2 T_2^2}{1 + (\gamma B_x)^2 T_1 T_2 + (\omega_0 - \omega)^2 T_2^2} S_z^{eq} \qquad (5.34)$$

These components $S_i(\omega)$ can be rewritten in terms of their respective magnetic susceptibilities $\chi_i(\omega)$

$$S_x(\omega) = \chi_x(\omega)\hbar\gamma B_x \qquad (5.35)$$

$$S_z(\omega) = \chi_z(\omega)\hbar\gamma B_z \qquad (5.36)$$

The susceptibilities $\chi_x(\omega)$ and $\chi_z(\omega)$ are described by two different processes. $\chi_x(\omega)$ describes the resonant response of the spins to the alternating perturbation field, while $\chi_z(\omega)$ has the typical form of a relaxation process [7]. The problem can be converted from a spin ensemble to a TLS ensemble using the correspondence in Eq 5.23. For the TLS problem, an analogous electric $\overset{=}{\chi}_{res}$ (resonant process) and relaxation $\overset{=}{\chi}_{rel}$ susceptibility tensor can be defined. In response to an external electric field, the average of the dipole moments is given by

$$\langle p_x \rangle = \overset{=}{\chi}_{res}(\omega) \cdot \vec{E} \qquad (5.37)$$

$$\langle p_z \rangle = \overset{=}{\chi}_{rel}(\omega) \cdot \vec{E} \qquad (5.38)$$

using Eq 5.32 - 5.34, the explicit forms of $\chi_{res}^=$ and $\chi_{rel}^=$ are given by [45]

$$\chi_{res}^= = -\frac{\sigma_z^0}{\hbar}\left(\frac{1}{\omega_0 - \omega + iT_2^{-1}} + \frac{1}{\omega_0 + \omega - iT_2^{-1}}\right)p_x p_x \qquad (5.39)$$

$$\chi_{rel}^= = -\frac{d\sigma_z^{eq}}{dE}\left(\frac{1 - i\omega T_1}{1 + \omega^2 T_1^2}\right)p_z p_z \qquad (5.40)$$

where

$$\sigma_z^0(E) = \frac{1 + (\omega_0 - \omega)^2 T_2^2}{1 + \Omega_R^2 T_1 T_2 + (\omega_0 - \omega)^2 T_2^2}\sigma_z^{eq}(E) \qquad (5.41)$$

$$\sigma_z^{eq} = -\tanh(E/2k_b T) \qquad (5.42)$$

Here the Rabi frequency $\Omega_R = 2p_x \cdot \vec{E}$ for the TLS has been introduced. For the TLS, T_1^{-1} refers to the relaxation rate for an ensemble of TLS in a non-equilibrium state to relax to its equilibrium value. This mechanism occurs through interaction (absorption and emission) with the phonon bath. T_2 processes are a result of TLS-TLS mutual interactions.

5.3 TLS Contribution to Dielectric Loss

Superconducting microwave resonators typically operate at frequencies of $\omega \sim 10^9$ and temperatures of < 1 K. Under these conditions, the effect of the TLS on the dielectric constant is dominated by the resonant $\chi^{=}_{res}$ term in Eq 5.39, where the relaxation term in Eq 5.40 is much smaller and can be neglected. The TLS effect on the dielectric constant can be found by integration over all dipole orientations of the TLS parameters [48]

$$\epsilon_{TLS}(\omega) = \epsilon'_{TLS}(\omega) - i\epsilon''_{TLS}(\omega) = \iiint d\Delta d\Delta_0 d\hat{p} \frac{P_0}{\Delta_0} \hat{p} \cdot \chi^{=}_{res} \cdot \hat{p} \tag{5.43}$$

Where Δ is the TLS asymmetry, Δ_0 is the TLS tunnel splitting and P_0 is the two-level density of states. For weak electric fields and $\Omega_R^2 T_1 T_2 \ll 1$, a change of variables in Eq. 5.43 reduces to an energy integral of the form [7]

$$\epsilon_{TLS}(\omega) = \frac{P_0 p_0^2}{3\hbar} \int_0^{E_{max}} \chi^{=}_{res}(\omega) dE \tag{5.44}$$

$$= \frac{2P p_0^2}{3} \left(\Psi\left(\frac{1}{2} - \frac{\hbar\omega - i\hbar T_2^{-1}}{2i\pi k_B T} \right) - \log\left(\frac{E_{max}}{2\pi k_B T} \right) \right) \tag{5.45}$$

where Ψ is the complex digamma function and E_{max} is the maximum energy splitting of the TLS. Furthermore, it can be shown that the temperature variation of the dielectric constant is given by [39]

$$\frac{\epsilon'_{TLS}}{\epsilon} = -\frac{2\delta_{TLS}^0}{\pi} \left[Re\Psi\left(\frac{1}{2} - \frac{\hbar\omega}{2\pi i k_B T} \right) - \log\left(\frac{\hbar\omega}{2\pi k_B T} \right) \right] \tag{5.46}$$

where $\delta_{TLS}^0 = \pi P p_0^2 / 3\epsilon$ is the zero temperature, TLS-induced dielectric loss tangent for weak electric fields. Using the property $Im\Psi(1/2 + iy) = \pi/2 \tanh(\pi y)$ [49] the TLS contribution to the dielectric loss tangent is given by

$$\delta_{TLS} = \frac{\epsilon''_{TLS}(\omega)}{\epsilon} = \delta_{TLS}^0 \tanh\left(\frac{\hbar\omega}{2k_B T} \right) \tag{5.47}$$

The TLS contribution to the dielectric constant can be measured indirectly by the fractional change in the resonant frequency of the resonator as a function of temperature [41]

$$\frac{\Delta f_r}{f_r} = -\frac{F}{2}\frac{\Delta\epsilon_{TLS}}{\epsilon} \tag{5.48}$$

where F is a filling factor given by

$$-\frac{\int_{v_h} \epsilon'_{TLS}|\vec{E}|^2 d\vec{r}}{\int_V \epsilon|\vec{E}|^2 d\vec{r}} = \frac{E_{TLS}}{E_{tot}} \tag{5.49}$$

which accounts for the fact that the TLS host may only partially fill the resonator geometry, giving a reduced effect on the change in resonant frequency. The filling factor F is simply the ratio of energy stored in the TLS host to the total energy stored in the resonator. Using Eq 5.46, Eq. 5.48 can be written explicitly as

$$\frac{f_r(T) - f_r(0)}{f_r} = \frac{F\delta^0_{TLS}}{\pi}\left[Re\Psi\left(\frac{1}{2} - \frac{\hbar\omega}{2j\pi k_b T}\right) - \log\frac{\hbar\omega}{2\pi k_b T}\right] \tag{5.50}$$

Similarly, if the internal loss of the resonator is dominated by the TLS induced dielectric loss δ_{TLS} (Eq 5.47), then the internal quality factor will have a temperature dependence given by

$$\frac{1}{Q_i(T)} = F\delta^0_{TLS}\tanh\left(\frac{\hbar\omega}{2k_b T}\right) \tag{5.51}$$

Equations 5.50, 5.51 can be applied directly to the experimental results described in the next chapter to estimate the zero temperature dielectric loss tangent δ^0_{TLS}.

Chapter 6

Experimental Details

6.1   Sample and Cryostat Preparation

The measured device was a CPW resonator containing amorphous silica ($SiO_{2)}$ provided by *D-Wave Systems, Inc.* The resonant frequency of the device f_r was measured to be 5.5 GHz. Sweeping the input drive power to the resonator from the -140 dBm to -65 dBm, Q_r (Q_c) ranged from 160 (540) to 820 (840).

The device was securely mounted with *General Electric* (GE) varnish in an rf-tight, gold-plated solid copper enclosure. This enclosure is shown in Figure. 6.1. An ultrasonic wire bonder was used to connect 1 Mil aluminum wires from the printed circuit board (PCB) to the device under test. These bonds were kept as short as possible to reduce impedance mismatches from the PCB to the device. The enclosure was securely fastened to the experimental stage (polished copper plate) located at the bottom of the cryostat. This experimental stage is connected to the mixing chamber by two copper straps. A resistive heater (500 Ω) mounted on the experimental stage is used to temperature-control the device. The copper straps provide a weak thermal link to the mixing chamber, enabling swift changes in the stage temperature and stable operation of the DR.

The input transmission line has a series of attenuators thermally linked to the various cold stages to reduce room temperature noise at the input of the device. In total,
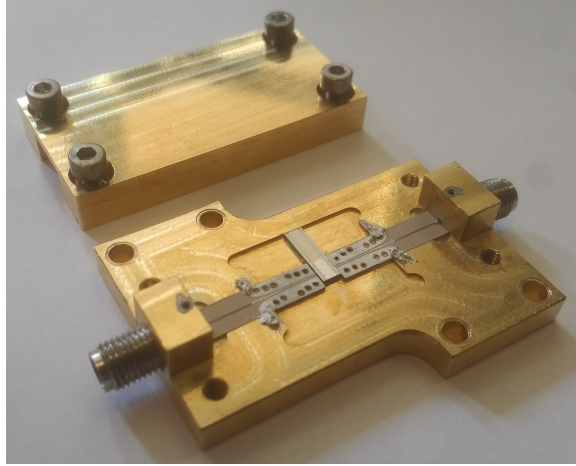
Figure 6.1: Gold-plated copper enclosure used for the resonator measurement. Designed and machined by *D-Wave Systems, Inc.*

50 dB of attenuation is used to reduce 300 K (broadband) noise to approximately the base temperature of the DR (75 mK) at the input of the device. Rigid, superconducting niobium-titanium (NbTi) coaxial cables are used to thermally isolate the PTR 2nd stage from the experimental stage. A cryogenic low noise amplifier (LNA), mounted on the PTR 2nd stage, is employed to amplify the transmission through the device. The LNA (CITCRY01-12A) is a high electron-mobility transistor (HEMT) amplifier. The high mobility is created by a two-dimensional electron gas (2DEG), typically formed using an GaAs/AlGaAs heterostructure. According to the specification sheet, the LNA has a noise temperature of 3.5 K and a gain of 33 dB at 5.5 GHz. In addition, a room temperature amplifier stage was implemented consisting of two identical amplifiers (2X Mini-Circuits, model ZX60-24-S+) which have a noise temperature of $\sim$ 1700 K and a gain of 24 dB at 5.5 GHz. The noise temperature of the amplifier chain can be calculated from the Friis equation

$$T_{sys} = T_1 + \frac{T_2}{G_1} + \frac{T_3}{G_1 G_2} + ... \tag{6.1}$$

where T_1, T_2, T_3 are the noise temperatures of the first, second and third stage amplifiers

and G_1, G_2 are the power gains of the first and second stage amplifiers. For this system, the resulting noise temperature referred to the input is ~ 4.7 K, dominated by the HEMT amplifier. A vector network analyzer (VNA) was used to measure the transmission S_{21} through the device and amplifier chain. A schematic of the microwave circuit is shown in Fig. 6.2.
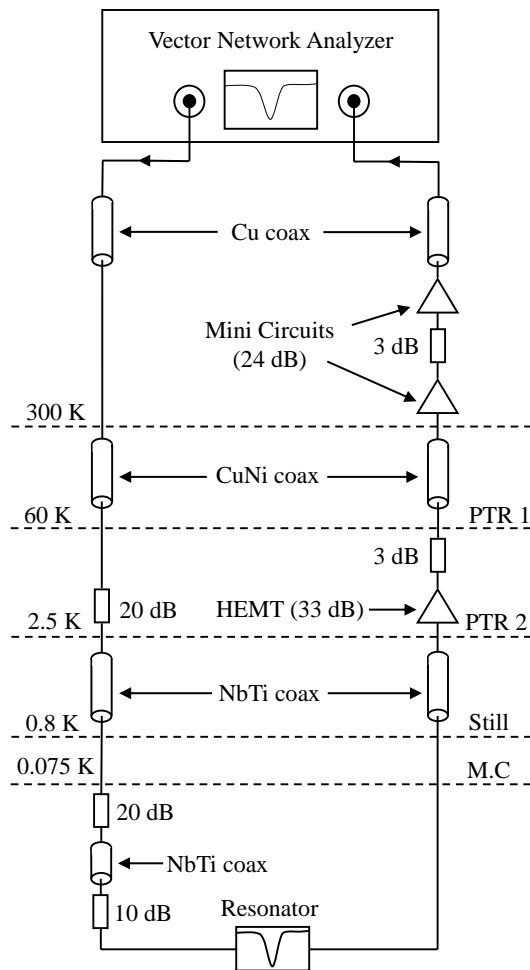

Figure 6.2: Schematic of the microwave circuit set up on the dry DR for measurements on superconducting resonators.

6.2   Fitting Procedures

Several methods exist to extract the quality factor Q_r and resonant frequency f_r of microwave resonators [50]. The accuracy of the different methods depends on the order of magnitude of the Q_r and the signal to noise ratio (SNR). The "3 dB method" is one of the simplest techniques, using only discrete points from the magnitude of the transmission data $|S_{21}|$ as a function of frequency. For this method, the resonant frequency f_r is determined from the minimum transmission frequency. The half power $1/\sqrt{2}$ points (3 dB in log scale) on either side of the resonance dip determine the bandwidth Δf_{3dB}. The quality factor is then given by

$$Q_r = f_r/\Delta f_{3dB} \tag{6.2}$$

While this method is simple, it generally gives poor results for noisy and/or asymmetric resonance data. For realistic experimental conditions, the resonance data becomes skewed. This is caused by crosstalk between transmission lines and coupling structures, impedance mismatches between coupling ports and the measurement device, and noise. Furthermore, without the phase information, the loss from the total quality factor Q_r cannot be divided into loss arising from coupling to the feedline Q_c and internal Q_i mechanisms. Instead, the most robust method for extracting the resonance parameters is a non-linear least-squares fit of the phase vs frequency of the complex t_{21} data [50]. This technique is capable of accurately measuring values of Q_r over many decades from lossy devices with Q_r <10^3 to state of the art Q_r >10^6. In this work, transmission data is collected from a VNA. Data analysis and fitting of the data was written in Python programming language. The following procedure closely follows that outlined by Gao [41].

To fit the data according to a phase vs frequency fit, the cable delay τ of the circuit must first be quantified and programmed into the VNA using the 'electrical delay' feature. To determine the delay, the frequency on the VNA was adjusted to be measuring off-resonance of the device. The VNA was then set to measure the expanded phase as a function of frequency. For off-resonance frequencies, the expanded phase is linear, decreasing with frequency as a result of the wavelength increasing. The cable delay τ can then be

determined from the slope of the expanded phase as a function of frequency

$$\tau = \frac{\text{slope } \theta(\text{f})}{360°} \tag{6.3}$$

For this system, the cable delay was determined to be 32 ns. At the resonant frequency ($\sim$ 5.5 GHz), real and complex transmission data was collected in polar format. In the complex polar plane, t_{21} traces out a resonance circle. A fit is used to determine the circle center $z_c = x_c + iy_c$. Using the fitted center z_c, the data is rotated and translated to origin using the following transformation

$$z' = (z_c - z)\exp^{-j\alpha} \tag{6.4}$$

Next, the phase angle θ (with respect to the positive real axis) of the transformed data z' is fit to the following profile

$$\theta = -\theta_0 + 2\tan^{-1}[2Q_r(1 - \frac{f}{f_r})] \tag{6.5}$$

A non-linear least-squares minimization of Eq 6.5 can be performed using the *lmfit* package in Python (see Appendix C)

$$\min\left[\sum_{i=1}^{n}\left| -\theta_0 + 2\tan^{-1}[2Q_r(1 - \frac{f}{f_r})\right|^2\right] \tag{6.6}$$

where f_r, Q_r, and θ_0 are determined from the fit. The geometric relationship between these parameters is illustrated in Fig. 6.4. Furthermore, the parameters Q_c and θ_0 are given by

$$Q_c = \frac{|z_c| + r}{2r}Q_r \tag{6.7}$$

and ϕ_0 is related to θ_0 by

$$\phi_0 = \theta_0 - \arg(z_c) \tag{6.8}$$
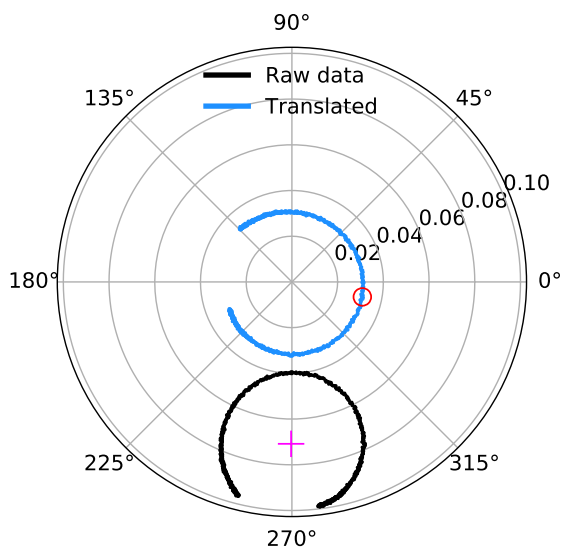
(a) Polar plot ($\mathrm{Im}(S_{21})$ vs $\mathrm{Re}(S_{21})$) of raw data (black) and transformed (blue).
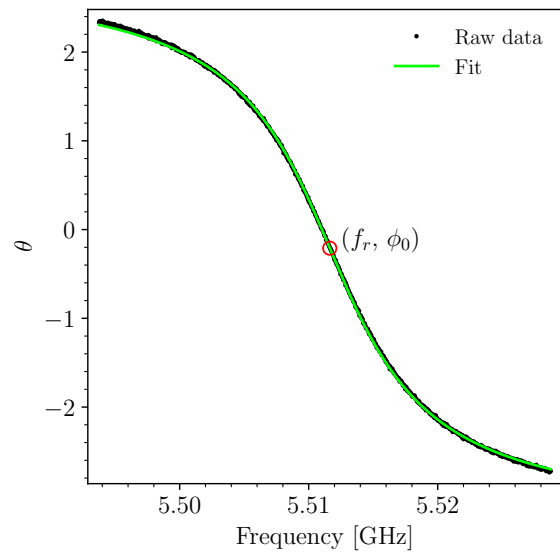
(b) Phase as a function of frequency of the raw and fitted data.

Figure 6.3: Non-linear least-squares fit of the phase vs frequency of the complex t_{21} data.
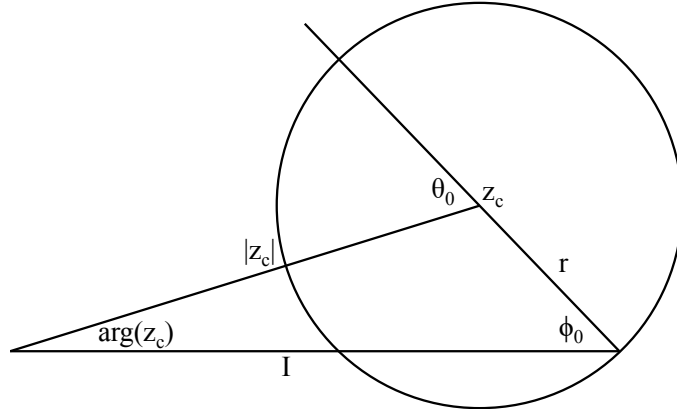
Figure 6.4: Geometric relationship between parameters to determine Q_c and ϕ_0. Figure Adopted from [7].

The SNR of the measured data is determined by the fitted resonance circle generated by plotting the real and complex transmission data, as shown in Fig. 6.3 (a). The distance d_i of each data point to the center (x_c, y_c) of the fitted resonance circle is calculated from

$$d_i = \sqrt{(x_i - x_c)^2 + (y_i - y_c)^2} \tag{6.9}$$

The SNR is then defined by

$$SNR = \frac{r_{circle}}{\sqrt{\frac{1}{N} \sum_{i=0}^{N} (d_i - r_{circle})^2}} \tag{6.10}$$

To extract accurate resonance parameters, the SNR of the transmission data must be kept above 10 (10 dB) [50]. For the data presented in Section 6.3, the SNR was kept above 40 (16 dB) to ensure accurate resonance parameters were extracted from fitting. If the SNR is maintained above 10 dB, To reduce the noise in the measurement, the VNA was set to a resolution bandwidth of 100 Hz, with 10 averages of each frequency sweep for a single data point. For a typical frequency span of 40 MHz, each data point took $\sim$ 30 minutes to collect.

80

6.2.1 Lorentzian Fit

In addition, a Lorentzian fit was performed on the raw $|t_{21}|$ data. The lorentzian fit is the second most accurate method for Q_r and f_r [50]. This was done to ensure the correct resonance frequency and quality factor were extracted from the phase vs frequency fit. For the data collected, the values of Q_r and f_r extracted from the two methods agree within less than 5% for Q_r and less than 1% for f_r. The data was fit to a Lorentzian with the following model [50]

$$|t_{21}|^2 = A_1 + A_2(f - f_r) + \frac{A_3 + A_4(f - f_r)}{1 + 4Q_r^2 \frac{f - f_r}{f_r}} \tag{6.11}$$

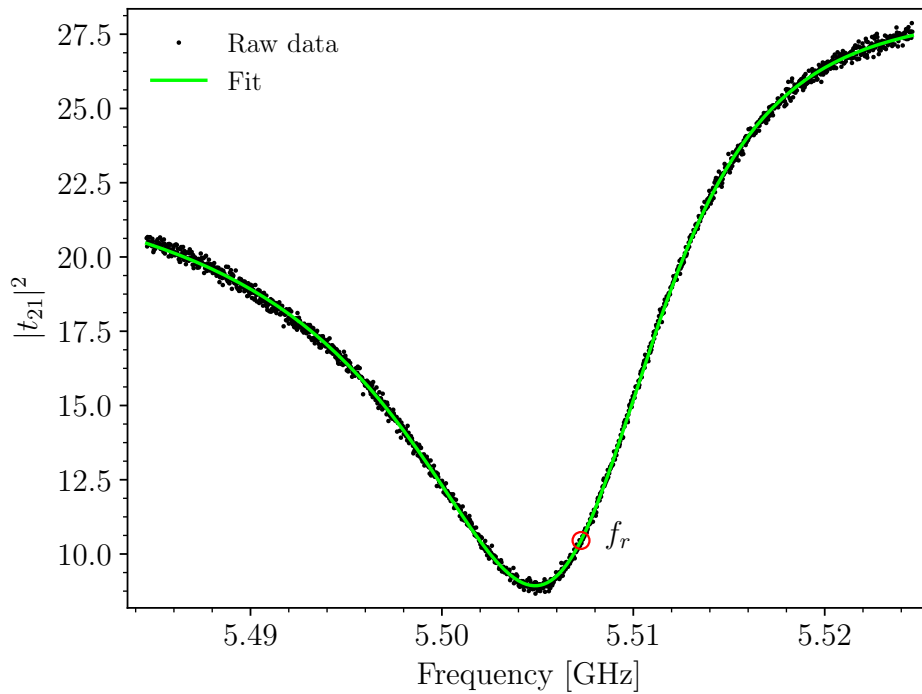Figure 6.5: Skewed Lorentzian fit to $|t_{21}|$ data at T = 300 mK. Note the highly asymmetric line shape. The red circle indicates the fitted resonance frequency which does not occur at the minimum transmission frequency due to the asymmetry [5].

6.3 Experimental Results

Using the experimental setup outlined previously, measurements were performed on a CPW resonator containing amorphous SiO_2. Both magnitude S_{21} and complex t_{21} data were collected using a VNA. The complex t_{21} data was fitted to a phase vs frequency fit to extract the resonance frequency f_r, total quality factor Q_r, coupling quality factor Q_c and internal quality factor Q_i. For this device at base temperature of 75 mK, values of Q_r ranged from ~ 200 at the lowest readout power measured (-140 dBm) to ~ 850 for the highest readout power measured (-65 dBm).

6.3.1 Power Dependence

Fitting to the TLS model requires temperature dependence of the resonator in the single microwave photon regime (see Appendix B). Thus, the readout power dependence of the resonator must first be characterized to determine this regime. Measurements of f_r and Q_i were performed at base temperature (75 mK). Fig. 6.6 shows the raw transmission $|S_{21}|$ data for several readout powers. A very small decrease (< 250 kHz) in resonant frequency f_r is observed for increasing readout power. For the majority of readout powers plotted ($> $ -120 dBm), the TLSs are being saturated by the high flux of microwave photons.
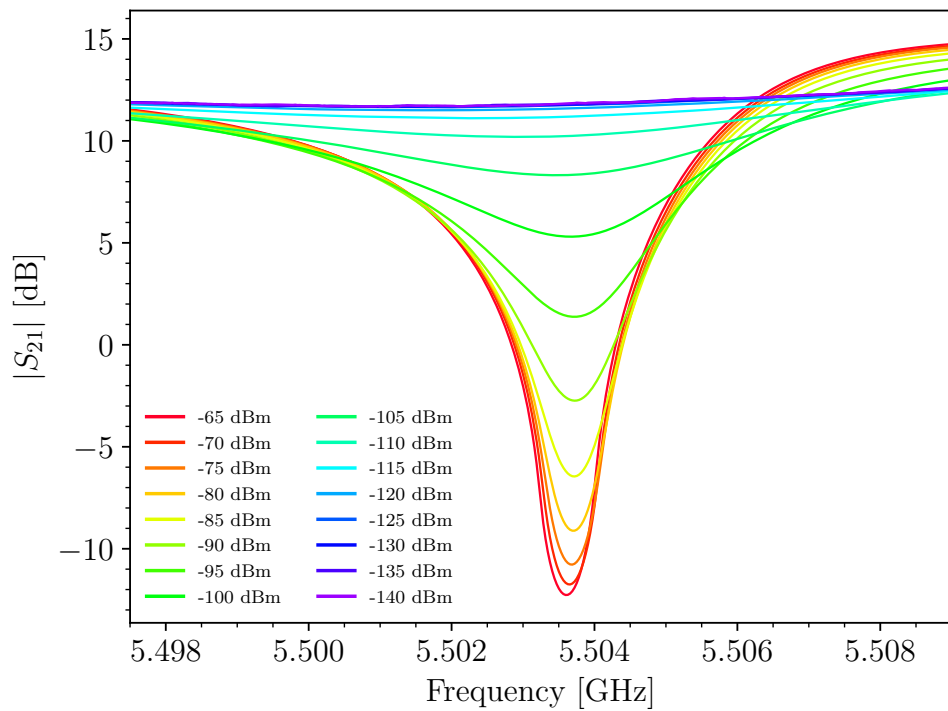
Figure 6.6: Transmission $|S_{21}|$ as a function of frequency for several readout powers. P_{int} ranges from -65 dBm to -140 dBm in steps of 5 dBm.

Using the full (real and imaginary) t_{21} data, the internal quality factor Q_i^{-1} can be extracted as a function of readout power (Fig. 6.7). Two regimes are observed. For readout powers below -120 dBm, Q_i^{-1} begins to level-off to a high value. This plateau in Q_i^{-1} correlates to maximum dissipation (loss) caused by the TLS. Above -120 dBm, Q_i^{-1} decreases with readout power scaling as $P_{int}^{-0.5}$, which is caused by saturation of the TLS fluctuators. To maintain a reasonable SNR of greater than ~ 17 dB, temperature dependence data in the following section was collected at a readout power of -130 dBm, still within the single photon regime.

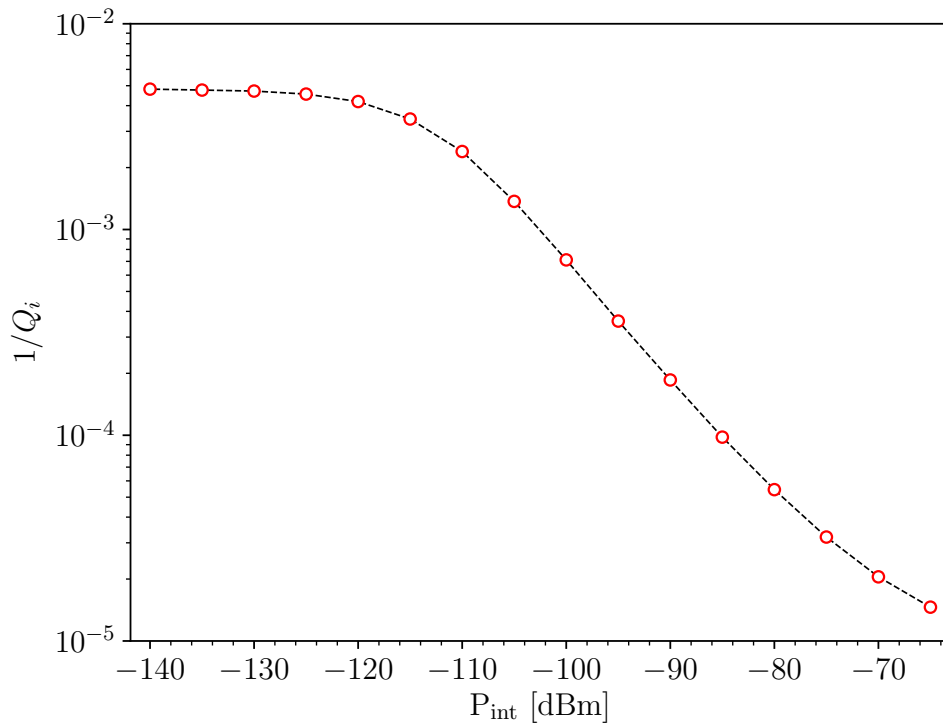Figure 6.7: Internal loss Q_i^{-1} as a function of readout power P_{int}. Q_i^{-1} extracted from a phase vs frequency fit. P_{int} ranges from -65 dBm to -140 dBm in steps of 5 dBm.

6.3.2 Temperature Dependence

Next, the temperature dependence of the resonator properties was characterized. For a fixed readout power of -130 dBm, the bath temperature was varied from base temperature of 75 mK to 500 mK. The data density was higher at lower temperatures ($\sim$ 100 mK) where the TLS are thermally activated. Figure 6.8 shows the raw transmission $|S_{21}|$ data for several bath temperatures. The broadness of the resonance is observed to decrease with increasing temperature as a result of the TLS becoming saturated by their interaction with the phonon bath. The saturation of the TLS with increasing temperature results in an increase of the internal quality factor Q_i. In addition, the resonant frequency f_r is observed to shift to higher values with increasing temperature, which is consistent with the TLS model.
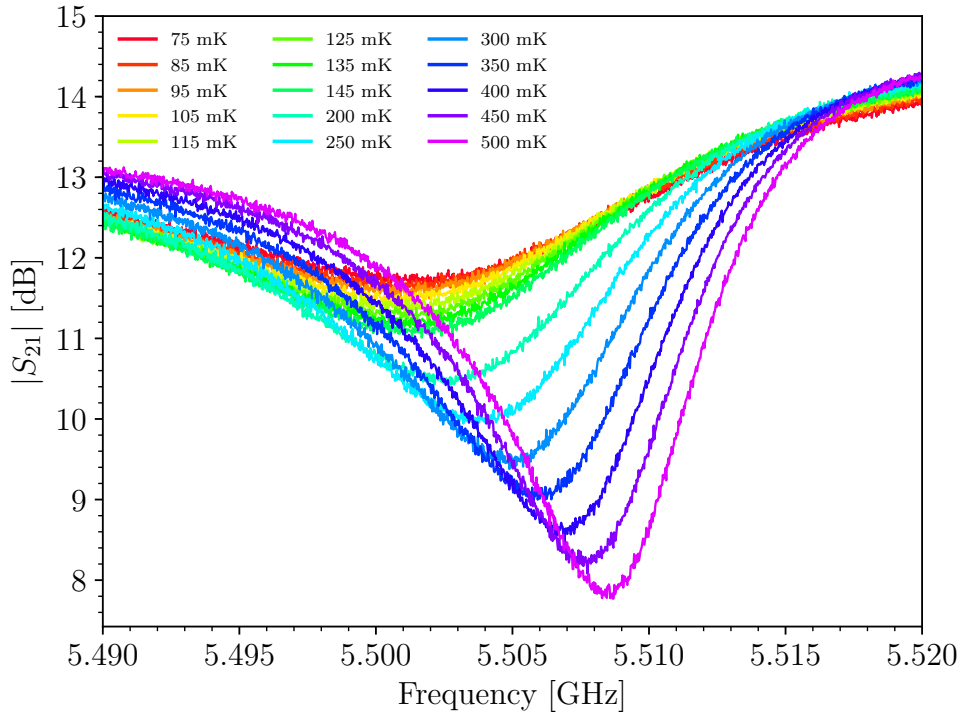

Figure 6.8: Transmission $|S_{21}|$ as a function of frequency for several bath temperatures. T ranges from base temperature 75 mK to 500 mK.

Using the full complex t_{21} data, the internal loss Q_i and resonant frequency f_r can be extracted as a function of temperature. Fig. 6.9 shows the change in resonant frequency as a function of temperature. Over the full temperature span, the resonant frequency f_r changes by ~ 5 MHz. The non-monotonic nature of frequency shift and thus dielectric constant is consistent with the TLS model. From Eq. 5.50, for $T > \hbar\omega/2k_B \sim 120$ mK, f_r decreases (ϵ increases) with decreasing temperature; at $T = \hbar\omega/2k_B \sim 120$ mK, a minimum in f_r (maximum in ϵ) occurs, while at temperatures below ~ 120 mK, f_r begins to increase again (ϵ decreases).
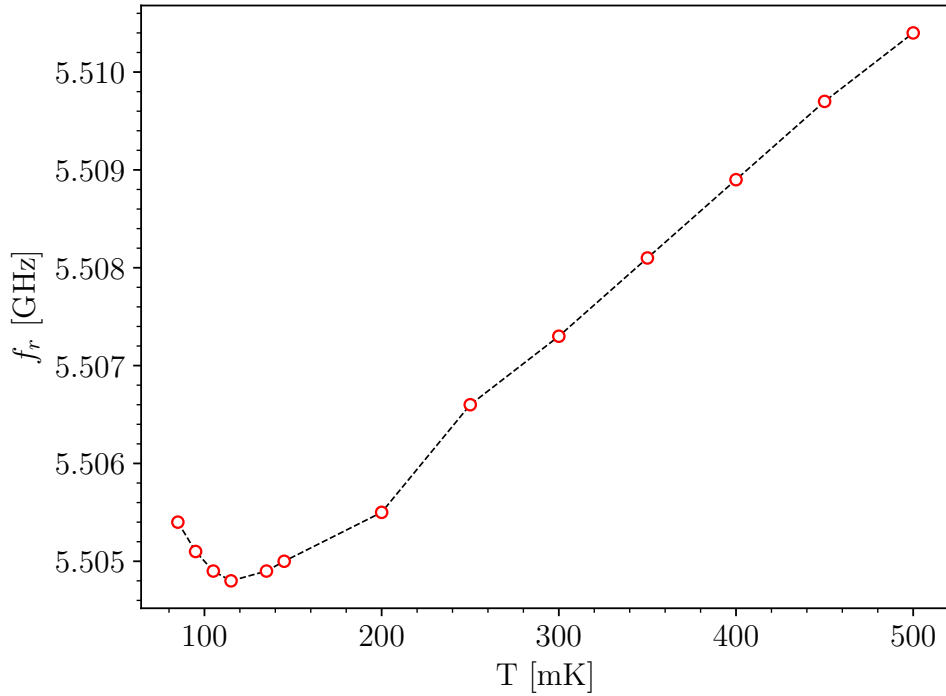
Figure 6.9: Resonant frequency f_r as a function of bath temperature.

To obtain the value of the zero temperature dielectric loss tangent δ_{TLS}^0, the data for the resonant frequency f_r as a function of temperature was fit to its theoretical profile Eq. 5.50. A plot of the fractional frequency shift as a function of temperature is shown in Fig. 6.10. As a result of the fit, the value for δ_{TLS}^0 (up to a filling factor F) is 4.4 x 10^{-3}.

The δ^0_{TLS} can also be obtained by fitting the internal loss as a function of temperature to its theoretical profile Eq. 5.51. This is shown in Fig. 6.11, where the value for δ^0_{TLS} (up to a filling factor F) obtained is 4.9 x 10^{-3}. The values of δ^0_{TLS} obtained from these two methods agree within $\sim$ 10%. From literature, typical values for δ^0_{TLS} are in the range 10^{-4} to 10^{-2} for amorphous materials [40].

Figure 6.10: Fractional resonant frequency shift as function of temperature fit to its theoretical profile Eq. 5.50.

Figure 6.11: Internal loss Q_i^{-1} as function of temperature fit to its theoretical profile Eq. 5.51.
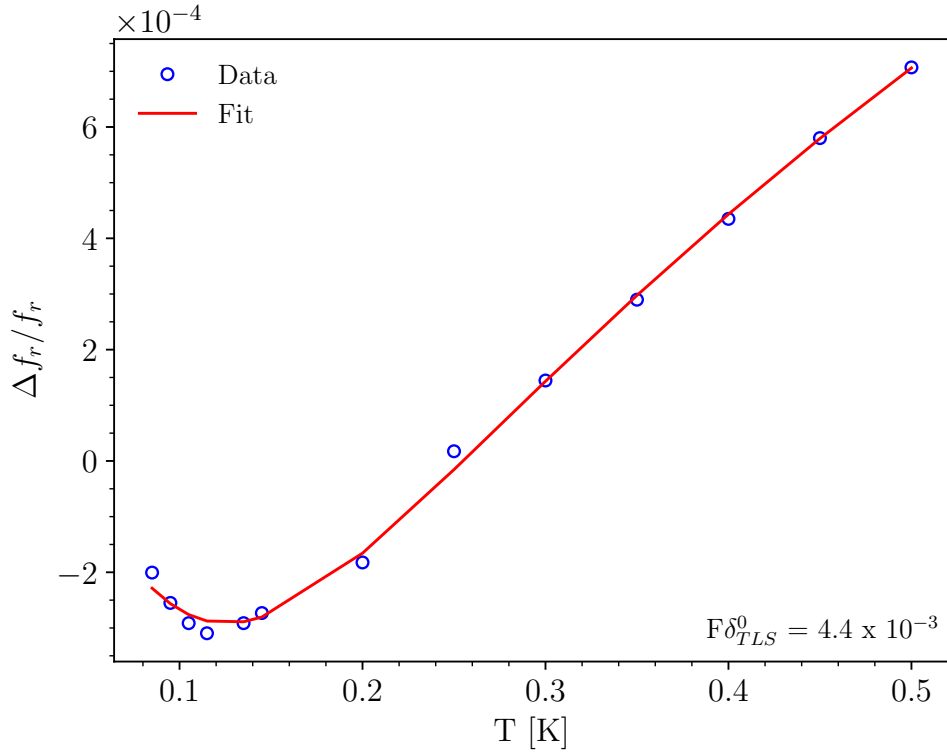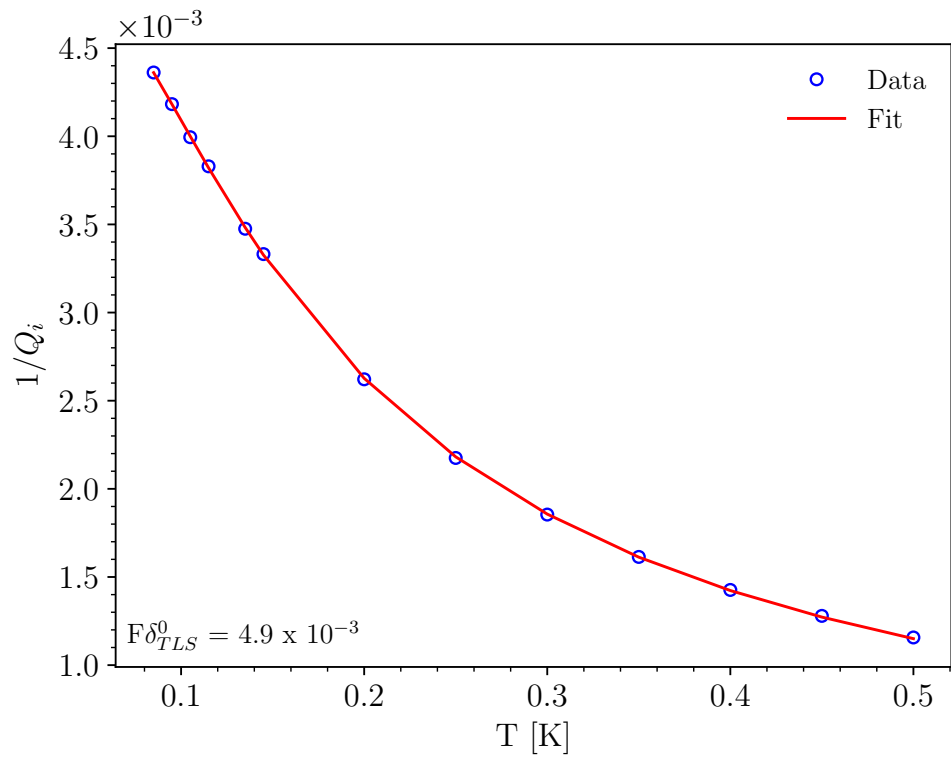
6.3.3 Summary

To accurately measure δ_{TLS}^0 in these devices requires a cryostat capable of reaching a base temperature of less than 100 mK, with 50 mK or less being more ideal. On the input drive line inside the cryostat, sufficient attenuation must be employed to suppress room temperature (300 K) broadband noise down to the base temperature of the cryostat. The device must be sealed in an a electromagnetically shielded enclosure to prevent any stray radiation from interacting with the device. A cryogenic LNA must be employed to amplify the transmission through the device. Room temperature amplifier stages can be used to further increase the SNR. The resonance parameters can be extracted by performing a non-linear least-squares fit of the phase vs frequency of the complex t_{21} data from a VNA.

6.4   Conclusions

In summary, a measurement system was configured to perform ultra low temperature characterization of superconducting resonators. This included the set up of a microwave circuit on the dry DR configured in Part I. Data analysis was performed in Python programming language. This analysis allowed for extraction of important resonance parameters and ultimately the key figure of merit for these devices, the zero temperature dielectric loss tangent δ_{TLS}^0. Measurements were done on a CPW resonator containing amorphous silicon dioxide. δ_{TLS}^0 for this resonator was found to be $\sim 4.6 \times 10^{-3}$, in agreement with values for amorphous materials from literature. With this characterization method, future studies of superconducting resonators can be performed. These future studies could explore different resonator designs, materials and fabrication methods. This will lead to a better understanding of how to reduce losses in these devices.

6.5   Future Work

Measurements at lower temperatures ≤ 75 mK would improve the fitting and ultimately the accuracy of δ_{TLS}^0. Additionally, the SNR could be increased by extending the integration

time of the measurement. This could be achieved by reducing the resolution bandwidth on the VNA from 100 Hz to 10 Hz and increasing the number of frequency sweep averages.

In the future, the experimental setup could be adapted to replace the VNA with a homodyne mixing technique [36]. A schematic of such a setup is shown in Figure 6.12. VNAs have a large measurement overhead and are restrictive in the types of measurements that can be performed. In contrast, the homodyne mixing technique is a faster, more flexible method of measuring the transmission through the resonator. For this method, the output of a microwave generator is split equally using a balanced power splitter. One branch is sent to the input of the resonator and the other branch is sent to the LO port of the IQ mixer. Just as before, the output of the resonator is amplified with cryogenic and room temperature amplifier stages. The amplified output is connected to the RF port of the IQ mixer. The IQ mixer is essentially two standard double balanced mixers, with one having a 90 degree phase shift applied to the LO port before mixing. The output of the mixer produces a real (in phase) component from channel I and an imaginary (quadrature) component from channel Q. The analog outputs can then be digitized quickly using a high resolution digitizer. Thus, the resolution and measurement time could be improved by using this technique.
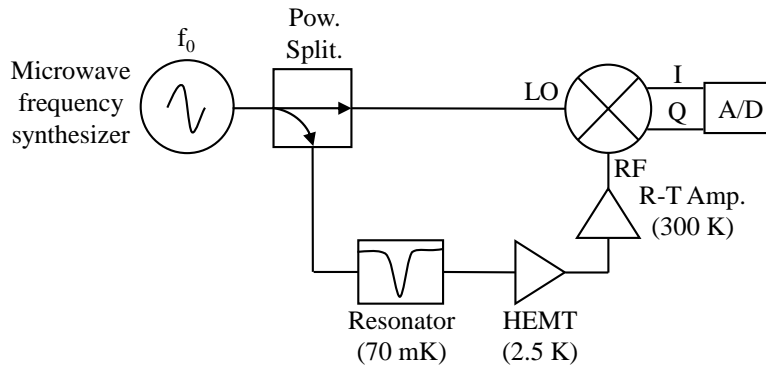

Figure 6.12: Homodyne mixing technique.

Chapter 7

Thesis Summary

Reiterating from the conclusion of Part I, the Shasta cryostat was successfully adapted from an adiabatic demagnetization refrigerator to a dry style dilution refrigerator. The dilution refrigerator outperforms the adiabatic demagnetization refrigerator in that it is able to provide continuous cooling power for temperatures above 70 mK. With 33 μW of heat applied to the mixing chamber, the dilution refrigerator is capable of regulating a base temperature of 100 mK indefinitely. In contrast, the adiabatic demagnetization refrigerator could sustain 33 μW of applied heat for $\leq$ 50 minutes before beginning to warm up. The poor base temperature of the dilution refrigerator was investigated and is consistent with a continuous heat load of 23 μW on the mixing chamber. The potential causes for the poor base temperature that were eliminated as a result of this work include: the ^{3}He return heat load, the phase boundary not being in the mixing chamber and internal issues with the *Oxford* 200 dilution unit. Other possibilities that could be investigated in the future include: self-heating of the resistance thermometers and vibrations from the pulse tube refrigerator and/or gas handling system.

The cryostat setup in Part I was crucial in Part II for the measurement system configured for characterizing superconducting microwave resonators. Reiterating from the conclusion of Part II, a microwave circuit was setup on the cryostat and data analysis was performed in Python programming language. With this measurement system, important resonance parameters along with the key figure of merit for these devices, the zero tem-

perature dielectric loss tangent δ^0_{TLS}, were extracted. Measurements on a CPW resonator containing amorphous silicon dioxide yielded a dielectric loss tangent of ~ 4.6 x 10^{-3}, in a agreement with values for amorphous materials found in literature. With this measurement system, future evaluation of superconducting resonators could explore different resonator designs, materials and fabrication methods. Detailed studies of these parameters will lead to a better understanding how to reduce losses for optimal resonator performance.

References

[1] High Precision Devices Inc. *Installation and Operation Manual.* HPD.

[2] Frank Pobell. *Matter and methods at low temperatures*, volume 2. Springer, 1996.

[3] John F O'Hanlon. *A user's guide to vacuum technology.* John Wiley & Sons, 2005.

[4] Pfeiffer Vacuum. *The Vacuum Technology Book, Volume II.*

[5] MS Khalil, MJA Stoutimore, FC Wellstood, and KD Osborn. An analysis method for asymmetric resonator transmission applied to superconducting devices. *Journal of Applied Physics*, 111(5):054510, 2012.

[6] C. Enss and S. Hunklinger. *Tunneling systems. In Low-Temperature Physics*, volume 1. Springer, 2005.

[7] Jiansong Gao. *The physics of superconducting microwave resonators.* PhD thesis, California Institute of Technology, 2008.

[8] Andreas Wallraff, David I Schuster, Alexandre Blais, Luigi Frunzio, R-S Huang, Johannes Majer, Sameer Kumar, Steven M Girvin, and Robert J Schoelkopf. Strong coupling of a single photon to a superconducting qubit using circuit quantum electrodynamics. *Nature*, 431(7005):162, 2004.

[9] Erik A Tholén, Adem Ergül, Evelyn M Doherty, Frank M Weber, Fabien Grégis, and David B Haviland. Nonlinearities and parametric amplification in superconducting coplanar waveguide resonators. *Applied physics letters*, 90(25):253509, 2007.

[10] J Schlaerth, A Vayonakis, P Day, J Glenn, J Gao, S Golwala, S Kumar, H LeDuc, B Mazin, J Vaillancourt, et al. A millimeter and submillimeter kinetic inductance detector camera. *Journal of Low Temperature Physics*, 151(3-4):684–689, 2008.

[11] Guglielmo Ventura and Lara Risegari. *The art of cryogenics: low-temperature experimental techniques*. Elsevier, 2010.

[12] William E Gifford and RC Longsworth. Pulse-tube refrigeration. *Trans. ASME*, 86:264–268, 1964.

[13] EI Mikulin, AA Tarasov, and MP Shkrebyonock. Low temperature pulse tube refrigeration. *Adv. in Cryogenic Engineering*, 29:629–637, 1984.

[14] Sadik Kakaç, MR Avelino, and Henry F Smirnov. *Low temperature and cryogenic refrigeration*, volume 99. Springer Science & Business Media, 2003.

[15] Zhu Shaowei, Wu Peiyi, and Chen Zhongqi. Double inlet pulse tube refrigerators: an important improvement. *Cryogenics*, 30(6):514–520, 1990.

[16] Heinz London, GR Clarke, and Eric Mendoza. Osmotic pressure of he 3 in liquid he 4, with proposals for a refrigerator to work below 1 k. *Physical Review*, 128(5):1992, 1962.

[17] P Das, R Bruyn de Ouboter, and KW Taconis. A realization of a london-clarke-mendoza type refrigerator. In *Low Temperature Physics LT9*, pages 1253–1255. Springer, 1965.

[18] Kurt Uhlig. 3he/4he dilution refrigerator with pulse-tube refrigerator precooling. *Cryogenics*, 42(2):73–77, 2002.

[19] Kurt Uhlig. 3he/4he dilution refrigerator with high cooling capacity and direct pulse tube pre-cooling. *Cryogenics*, 48(11-12):511–514, 2008.

[20] Kurt Uhlig. Condensation stage of a pulse tube pre-cooled dilution refrigerator. *Cryogenics*, 48(3-4):138–141, 2008.

[21] LE DeLong, OG Symko, and JC Wheatley. Continuously operating 4he evaporation refrigerator. *Review of Scientific Instruments*, 42(1):147–150, 1971.

[22] JR Clement and EH Quinnell. The low temperature characteristics of carbon-composition thermometers. *Review of Scientific Instruments*, 23(5):213–216, 1952.

[23] Adrian Bejan. Heat transfer. *Inc, Kanada*, 1993.

[24] Robert C Richardson, Eric N Smith, and Robert C Dynes. Experimental techniques in condensed matter physics at low temperatures. *Physics Today*, 42:126, 1989.

[25] WP Kirk and M Twerdochlib. Improved method for minimizing vibrational motion transmitted by pumping lines. *Review of Scientific Instruments*, 49(6):765–769, 1978.

[26] John Bardeen, Leon N Cooper, and J Robert Schrieffer. Microscopic theory of super-conductivity. *Physical Review*, 106(1):162, 1957.

[27] Brian David Josephson. Possible new effects in superconductive tunnelling. *Physics letters*, 1(7):251–253, 1962.

[28] David M Pozar. Microwave engineering, johnwiley & sons. *Inc., New York*, pages 367–368, 1998.

[29] Joris van Rantwijk, Martin Grim, Dennis van Loon, Stephen Yates, Andrey Baryshev, and Jochem Baselmans. Multiplexed readout for 1000-pixel arrays of microwave kinetic inductance detectors. *IEEE Transactions on Microwave Theory and Techniques*, 64(6):1876–1883, 2016.

[30] Anthony Megrant, Charles Neill, Rami Barends, Ben Chiaro, Yu Chen, Ludwig Feigl, Julian Kelly, Erik Lucero, Matteo Mariantoni, Peter JJ O'Malley, et al. Planar super-conducting resonators with internal quality factors above one million. *Applied Physics Letters*, 100(11):113510, 2012.

[31] Heinz London. Production of heat in supraconductors by alternating currents. *Nature*, 133(3361):497, 1934.

[32] John Bardeen, Leon N Cooper, and John Robert Schrieffer. Theory of superconductivity. *Physical review*, 108(5):1175, 1957.

[33] DC Mattis and John Bardeen. Theory of the anomalous skin effect in normal and superconducting metals. *Physical Review*, 111(2):412, 1958.

[34] AA Abrikosov, LP Gor'kov, and IM Khalatnikov. A superconductor in a high frequency field. *Sov. Phys. JETP*, 35:182, 1959.

[35] Jonas Zmuidzinas. Superconducting microresonators: Physics and applications. *Annu. Rev. Condens. Matter Phys.*, 3(1):169–214, 2012.

[36] Benjamin A Mazin. *Microwave kinetic inductance detectors*. PhD thesis, California Institute of Technology, 2005.

[37] P W Anderson, BI Halperin, and C M Varma. Anomalous low-temperature thermal properties of glasses and spin glasses. *Philosophical Magazine*, 25(1):1–9, 1972.

[38] WA Phillips. Tunneling states in amorphous solids. *Journal of Low Temperature Physics*, 7(3-4):351–360, 1972.

[39] WA Phillips. Two-level states in glasses. *Reports on Progress in Physics*, 50(12):1657, 1987.

[40] John M Martinis, Ken B Cooper, Robert McDermott, Matthias Steffen, Markus Ansmann, KD Osborn, Katarina Cicak, Seongshik Oh, David P Pappas, Raymond W Simmonds, et al. Decoherence in josephson qubits from dielectric loss. *Physical review letters*, 95(21):210503, 2005.

[41] Jiansong Gao, Miguel Daal, Anastasios Vayonakis, Shwetank Kumar, Jonas Zmuidzinas, Bernard Sadoulet, Benjamin A Mazin, Peter K Day, and Henry G Leduc. Experimental evidence for a surface distribution of two-level systems in superconducting lithographed microwave resonators. *Applied Physics Letters*, 92(15):152505, 2008.

[42] K Geerlings, S Shankar, E Edwards, L Frunzio, RJ Schoelkopf, and MH Devoret. Improving the quality factor of microwave compact resonators by optimizing their geometrical parameters. *Applied Physics Letters*, 100(19):192601, 2012.

[43] Thomas Cecil, Antonino Miceli, Orlando Quaranta, Chian Liu, Daniel Rosenmann, Sean McHugh, and Benjamin Mazin. Tungsten silicide films for microwave kinetic inductance detectors. *Applied Physics Letters*, 101(3):032601, 2012.

[44] SJ Weber, KW Murch, DH Slichter, R Vijay, and I Siddiqi. Single crystal silicon capacitors with low microwave loss in the single photon regime. *Applied Physics Letters*, 98(17):172510, 2011.

[45] Martin Otto. Low-temperature characterization of dielectric loss at microwave frequencies in aluminum oxide. Master's thesis, University of Waterloo, 2015.

[46] Felix Bloch. Nuclear induction. *Physical review*, 70(7-8):460, 1946.

[47] S. Hunklinger. Physical acoustics. *New York Academic Press*, volume 12, 1976.

[48] David P Pappas, Michael R Vissers, David S Wisbey, Jeffrey S Kline, and Jiansong Gao. Two level system loss in superconducting microwave resonators. *IEEE Transactions on Applied Superconductivity*, 21(3):871–874, 2011.

[49] Milton Abramowitz and Irene A Stegun. *Handbook of mathematical functions: with formulas, graphs, and mathematical tables*, volume 55. Courier Corporation, 1965.

[50] Paul J Petersan and Steven M Anlage. Measurement of resonant frequency and quality factor of microwave resonators: Comparison of methods. *Journal of applied physics*, 84(6):3392–3402, 1998.

[51] Ray Radebaugh. Development of the pulse tube refrigerator as an efficient and reliable cryocooler. In *Proceedings of Institute of Refrigeration*, volume 96, pages 1999–2000, 2000.

[52] Peter K Day, Henry G LeDuc, Benjamin A Mazin, Anastasios Vayonakis, and Jonas Zmuidzinas. A broadband superconducting detector suitable for use in large arrays. *Nature*, 425(6960):817, 2003.

[53] L Hilico, Claude Fabre, Serge Reynaud, and Elisabeth Giacobino. Linear input-output method for quantum fluctuations in optical bistability with two-level atoms. *Physical Review A*, 46(7):4397, 1992.

[54] Jay M Gambetta, Jerry M Chow, and Matthias Steffen. Building logical qubits in a superconducting quantum computing system. *npj Quantum Information*, 3(1):2, 2017.

[55] Shwetank Kumar, Jiansong Gao, Jonas Zmuidzinas, Benjamin A Mazin, Henry G LeDuc, and Peter K Day. Temperature dependence of the frequency and noise of superconducting coplanar waveguide resonators. *Applied Physics Letters*, 92(12):123503, 2008.

[56] Corey Rae McRae. Indium thin films in multilayer superconducting quantum circuits. 2018.

[57] Stefan Putz. *Circuit Cavity QED with Macroscopic Solid-State Spin Ensembles.* Springer, 2017.

[58] Oxford Instruments Limited. *Installation and Operation Manual.* Oxford.

Appendix A

Oxford 200 Dilution Unit Specifications

The commercial *Oxford* 200 dilution unit added to the cryostat in Chapter 3 has the following cooling power results, taken from the original operating manual.

Table A.1: *Oxford* 200 Dilution Unit Cooling Power Specifications [58].

Mixing Chamber Temperature (mK)	Mixing Chamber Cooling Power (μW)	^{3}He Flow Rate (μmols/sec)	Still Power (mW)
6.5	0	200	5.0
10.0	1	400	13
27.0	12	400	13
100 ± 10	37.3	400	13

Appendix B

Estimation of the Average Photon Number

In Chapter 6, the resonator is probed in what is known as a single microwave photon regime. To calculate the average number of photons in the resonator at any given time, the photon loss rate κ must first be determined. This is estimated by fitting the transmission data to a Lorentzian (see Section 6.2.1) and extracting the full width at half maximum (FWHM). For the data shown in Fig. 6.5, the loss rate is FWHM $= \kappa/2\pi \approx 1.45$ MHz. The average number of photons $\langle N \rangle$ for a drive amplitude P_{in} and frequency ω_c is given by [57]

$$\langle N \rangle = \frac{P_{in}}{\hbar \omega_c \kappa} \tag{B.1}$$

Using the photon loss rate κ, at microwave power of $P_{\text{in}} = -130$ dBm $= 10^{-16}$ W and a angular resonance frequency of $\omega_c = 2\pi \times 5.507$ GHz, the above equation yields $\langle N \rangle \approx$ 3.01. Thus, when the driving excitation and photon losses reach equilibrium, there are approximately 3 photons in the resonator.

Appendix C

Python Code for Fitting the Complex Transmission Data

The resonance parameters described in Chapter 7 are extracted using a non-linear phase versus frequency fit. The following is the Python code used to fit the complex transmission data and extract the resonance parameters.

```python
#Import Packages
import numpy as np
import matplotlib.pylab as plt
import os
from matplotlib import rc
import lmfit
from numpy import genfromtxt
#Change to Current Working Directory
os.chdir(os.getcwd())
#Global Variables
start = 200
stop = 1300
num_Points = stop - start
```

```python
All_Data=np.zeros((num_Points, 6))
theta = np.zeros(num_Points)
y_fit_corr = np.zeros(num_Points)
rot_theta = np.zeros(num_Points)
rot_theta_2 = np.zeros(num_Points)
difference = np.zeros(num_Points)
phase_shift =np.pi + 1.5
distance_SNR = np.zeros(num_Points)
sum_term = 0
lw = 1
#Read in Data
with open('Insert_Data_Name.csv') as f:
    lines = (line for line in f if not line.startswith('#'))
    data = np.loadtxt(lines, delimiter=',', skiprows=3)
#Seperate Data
x = data[start:stop, 1]
y = data[start:stop, 2]
R = np.sqrt(x**2 + y**2)
#Determine Quadrants
for w in range(0, num_Points):
    if (x [w] < 0 and y [w] > 0): #2
        theta [w] = (np.pi - abs(np.arctan(y[w]/x[w])))
    elif (x [w] > 0 and y [w] > 0): #1
        theta [w] = (abs(np.arctan(y[w]/x[w])))
    elif (x [w] < 0 and y [w] < 0): #3
        theta [w] = (np.pi + abs(np.arctan(y[w]/x[w])))
    elif (x [w] > 0 and y [w] < 0): #4
        theta [w] = (2*np.pi - abs(np.arctan(y[w]/x[w])))
#Organize into array
for i in range(0, num_Points):
    All_Data[i, 0] = data[i, 0]
```

```
        All_Data[i, 1] = data[i, 1]
        All_Data[i, 2] = data[i, 2]
        All_Data[i, 3] = R[i]
        All_Data[i, 4] = theta[i]
#Circle Fit
#Coordinates of the barycenter
x_m = np.mean(x)
y_m = np.mean(y)
#Calculation of the reduced coordinates
u = x - x_m
v = y - y_m
#Linear system defining the center (uc, vc) in reduced
#coordinates:
#Suu * uc +  Suv * vc = (Suuu + Suvv)/2
#Suv * uc +  Svv * vc = (Suuv + Svvv)/2
Suv  = sum(u*v)
Suu  = sum(u**2)
Svv  = sum(v**2)
Suuv = sum(u**2 * v)
Suvv = sum(u * v**2)
Suuu = sum(u**3)
Svvv = sum(v**3)
#Solving the linear system
A = np.array([ [ Suu, Suv ], [Suv, Svv]])
B = np.array([ Suuu + Suvv, Svvv + Suuv ])/2.0
uc, vc = np.linalg.solve(A, B)
xc_1 = x_m + uc
yc_1 = y_m + vc
#Calculate Distances from center (xc_1, yc_1)
Ri_1     = np.sqrt((x-xc_1)**2 + (y-yc_1)**2)
R_1      = np.mean(Ri_1)
```

```python
residu_1 = sum((Ri_1-R_1)**2)
center_R = np.sqrt(xc_1**2 + yc_1**2) #Radius of circle
if (xc_1 < 0 and yc_1 > 0): #2
    center_theta = (np.pi - abs(np.arctan(yc_1/xc_1)))
    arg_center_theta = np.pi - center_theta
elif (xc_1 > 0 and yc_1 > 0): #1
    center_theta = (abs(np.arctan(yc_1/xc_1)))
    arg_center_theta = center_theta
elif (xc_1 < 0 and yc_1 < 0): #3
    center_theta = (np.pi + abs(np.arctan(yc_1/xc_1)))
    arg_center_theta = np.pi + center_theta
elif (xc_1 > 0 and yc_1 < 0): #4
    center_theta = (2*np.pi - abs(np.arctan(yc_1/xc_1)))
    arg_center_theta = (2*np.pi) - center_theta
#End Circle Fit
#Apply Coordinate Shift
x_new = (x - xc_1)
y_new = (y - yc_1)
#Calculate SNR of Data
for h in range(0, num_Points):
    distance_SNR[h] = np.sqrt((((x[h] - xc_1)**2) + ((y[h] - yc_1)**2))
    sum_term = sum_term + (distance_SNR[h] - R_1)**2
SNR = R_1/(np.sqrt((1/num_Points)*sum_term))
print ('SNR: ' + str(SNR))
#Rotate Data
for d in range(0, num_Points):
    if (x_new [d] < 0 and y_new [d] > 0): #2
        rot_theta [d] = (np.pi -
                         abs(np.arctan(y_new[d]/x_new[d]))) + phase_shift
    elif (x_new [d] > 0 and y_new [d] > 0): #1
        rot_theta [d] = (abs(np.arctan(y_new[d]/x_new[d]))) + phase_shift
```

```python
        elif (x_new [d] < 0 and y_new [d] < 0): #3
            rot_theta [d] = (np.pi +
                            abs(np.arctan(y_new[d]/x_new[d]))) + phase_shift
        elif (x_new [d] > 0 and y_new [d] < 0): #4
            rot_theta [d] = (2*np.pi -
                            abs(np.arctan(y_new[d]/x_new[d]))) + phase_shift
        All_Data[d, 5] = rot_theta [d]
    for e in range(0, num_Points):
        test = ((All_Data [e, 5]/(2*np.pi)) -
                int(All_Data [e, 5]/(2*np.pi)))*(2*np.pi)
        if (test > 0 and test < np.pi):
            rot_theta_2 [e] = test
        elif (test > np.pi and test < 2*np.pi):
            rot_theta_2 [e] = (2*np.pi - test)*-1
        All_Data[e, 5] = rot_theta_2 [e]
    new_R = np.sqrt(x_new**2 + y_new**2)
    new_theta = -1*np.arctan(y_new/x_new)
    #Define fitting parameters
    p = lmfit.Parameters()
    p.add_many(('fr', 5*10**9), ('Qr', 100), ('t0', 1))
    #Set parameter limits
    p['t0'].set(min=-np.pi)
    p['t0'].set(max=np.pi)
    p['Qr'].set(min=0)
    p['Qr'].set(max=10000)
    p['fr'].set(min=5*10**9)
    p['fr'].set(max=6*10**9)
    #Function to be minimized
    def residual(p):
        v = p.valuesdict()
        return sum((All_Data[:, 5] + v['t0'] - 2*np.arctan(2*v['Qr']*
```

```python
                                        (1-(All_Data[:, 0]/v['fr'])))))**2)
mi = lmfit.minimize(residual, p, method='differential_evolution',
                                                nan_policy='omit')
lmfit.printfuncs.report_fit(mi.params, min_correl=0.1)
Zc = center_R
Qc = ((Zc + R_1)/(2*R_1))*float(mi.params['Qr'])
Qr_fit = float(mi.params['Qr'])
fr_fit = float(mi.params['fr'])
t0_fit = float(mi.params['t0'])
phi_0 = float(mi.params['t0']) - center_theta + phase_shift
Qi_inv = 1/(1/float(mi.params['Qr'])) - (1/Qc)
#Print All Results
print ('Circle Fit Results:')
print ('Radius: ' + str(R_1))
print ('Center (Xc, Yc): (' + str(xc_1) + ',' + str(yc_1) + ')')
print ('Center Theta: ' + str(center_theta))
print ('Qc: ' + str(Qc))
print ('1/Qi: ' + str(Qi_inv))
print ('Phi_0: ' + str(phi_0))
#Generate Fitted Data
def min_function(theta_0, total_Q, res_freq):
    angle = ((-1*theta_0 + 2*np.arctan(2*total_Q*
                                    (1-(All_Data[:, 0]/res_freq)))))
    return angle
y_fit = min_function(t0_fit, Qr_fit, fr_fit)
```